HHS Public Access

Author manuscript

Cell Stem Cell. Author manuscript; available in PMC 2024 April 06.

Published in final edited form as:

Cell Stem Cell. 2023 April 06; 30(4): 460–472.e6. doi:10.1016/j.stem.2023.02.010.

Hematopoietic Stem Cells Preferentially Traffic Misfolded Proteins to Aggresomes and Depend on Aggrephagy to Maintain Protein Homeostasis

Bernadette A. Chua[1], **Connor J. Lennan**[1], **Mary Jean Sunshine**[1], **Daniela Dreifke**[1], **Ashu Chawla**[2], **Eric J. Bennett**[3], **Robert A.J. Signer**[1,4,*]

[1]Division of Regenerative Medicine, Department of Medicine, Sanford Stem Cell Institute, Moores Cancer Center, University of California San Diego, La Jolla, CA, 92093 USA.

[2]La Jolla Institute for Immunology, La Jolla, CA, 92037 USA.

[3]Section of Cell and Developmental Biology, University of California San Diego, La Jolla, CA 92093, USA.

[4]Lead contact

SUMMARY

Hematopoietic stem cells (HSCs) regenerate blood cells throughout life. To preserve their fitness, HSCs are particularly dependent on maintaining protein homeostasis (proteostasis). However, how HSCs purge misfolded proteins is unknown. Here we show that in contrast to most cells that primarily utilize the proteasome to degrade misfolded proteins, HSCs preferentially traffic misfolded proteins to aggresomes in a Bag3-dependent manner, and depend on aggrephagy, a selective form of autophagy, to maintain proteostasis in vivo. When autophagy is disabled, HSCs compensate by increasing proteasome activity, but proteostasis is ultimately disrupted as protein aggregates accumulate and HSC function is impaired. *Bag3*-deficiency blunts aggresome formation in HSCs, resulting in protein aggregate accumulation, myeloid-biased differentiation, and diminished self-renewal activity. Furthermore, HSC aging is associated with a severe loss of aggresomes and reduced autophagic flux. Protein degradation pathways are thus specifically configured in young adult HSCs to preserve proteostasis and fitness, but become dysregulated during aging.

eTOC Blurb

*Correspondence: Robert A.J. Signer, UC San Diego Moores Cancer Center, 3855 Health Sciences Drive, La Jolla, CA 92093-0652, USA, Tel: 858-534-0732, rsigner@ucsd.edu, Twitter: @SignerLab.

AUTHOR CONTRIBUTIONS

B.A.C. and R.A.J.S. conceived the project, designed experiments, and wrote the manuscript. B.A.C. performed and analyzed all experiments. C.J.L. and D.D. provided technical support. M.S. supported mouse breeding. A.C. performed computational analysis. E.J.B. made critical intellectual contributions.

AUTHOR INFORMATION

The authors declare no competing interests.

Inability to grow HSCs in culture is a major barrier to their expanded use in cell-based therapies. Kruta et al. demonstrate that cultured HSCs rapidly increase protein synthesis, which severely disrupts proteostasis and impairs their self-renewal. Hsf1 activation promotes HSC fitness and proteostasis in culture and during aging in vivo.

Graphical Abstract

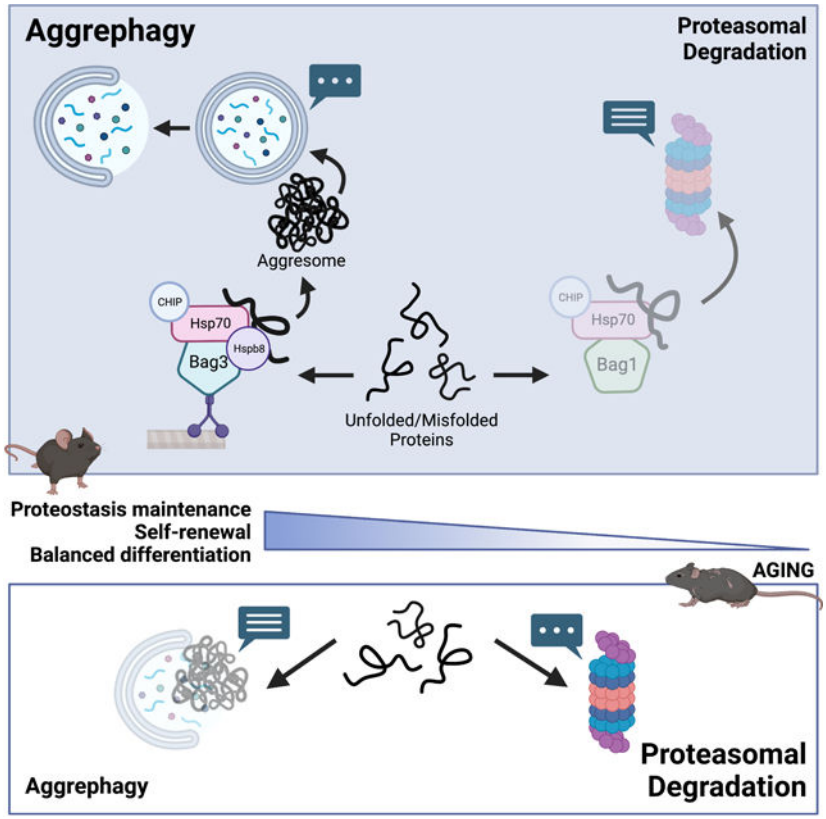

Keywords

stem cell; hematopoietic stem cell; autophagy; proteostasis; aggresome; proteasome; Bag3; aggrephagy; aging; protein degradation

INTRODUCTION

Maintenance of protein homeostasis (proteostasis) has emerged as fundamentally and preferentially important for stem cells[1]. Proteostasis disruption impairs stem cell self-renewal, which contributes to poor ex vivo expansion and is associated with degenerative disorders, cancer predisposition syndromes, and age-related pathologies in vivo[2–5]. To maintain proteostasis, cells employ a network of pathways to balance protein synthesis, folding, trafficking and degradation[6]. Despite being highly-conserved, the proteostasis network can be specifically configured to support stem cell fitness and longevity. Stem cells exhibit and depend on unusually low protein synthesis rates compared to restricted progenitors[7–11]. Modest increases in protein synthesis disrupt stem cell proteostasis and

impair self-renewal by increasing the biogenesis of misfolded proteins, but similar changes minimally impact progenitors[3]. Similarly, activation of the unfolded protein response (UPR) has dichotomous effects in stem and progenitor cells. UPR activation safeguards the integrity of the stem cell pool by preferentially inducing apoptosis in stressed stem cells, whereas it typically promotes an adaptive response in progenitors[12].

Protein degradation is a critical component of the proteostasis network[13]. Canonically, the ubiquitin proteasome system functions as the primary pathway for destruction of misfolded proteins[13]. In embryonic stem cells, high proteasome activity provides proteostasis buffering capacity by degrading and preventing accumulation of misfolded proteins[14]. In contrast, proteasome activity is low within some somatic stem cells like neural stem cells[15] and HSCs[3]. This raises a fundamental paradox: if somatic stem cells are highly dependent on proteostasis maintenance, why do they have such limited proteasome capacity to degrade misfolded proteins? We set out to address this question in HSCs and to uncover how protein degradation is configured to support stem cell proteostasis and function.

RESULTS

HSCs have high autophagic activity at steady state

To investigate protein degradation, we quantified proteasome activity within HSCs and progenitors. Consistent with prior studies[3,16], $CD150^+CD48^-Lineage^-Sca1^+ckit^+$ ($CD150^+CD48^-LSK$)[17] HSCs and $CD150^-CD48^-LSK$ multipotent progenitors (MPPs)[18,19] exhibited substantially less proteasome activity than common myeloid progenitors (CMPs), granulocyte macrophage progenitors (GMPs), megakaryocyte erythroid progenitors (MEPs), and common lymphoid progenitors (CLPs) (Fig. 1A, S1A). The paucity of proteasome activity prompted us to investigate whether HSCs utilize an alternative pathway to degrade misfolded proteins.

Macroautophagy (autophagy hereafter) is a bulk degradative process whereby organelles and macromolecules, including proteins, are recycled in a lysosomal-dependent manner[20]. In most cells, autophagy is minimally active at steady state, but is activated in response to starvation or stress[21]. In HSCs, autophagy is readily activated in response to cytokine withdrawal ex vivo[22], and promotes metabolic function, mitochondrial health and regulates cell signaling in vivo[22–26]. However, if/how autophagy contributes to HSC proteostasis is largely unexplored.

To measure autophagy in vivo, we used CAG-RFP-EGFP-LC3 mice[27]. LC3 is a cytosolic protein that when lipidated, localizes to the surface of autophagosomes[20]. To assess the frequency of HSCs and progenitors with autophagic activity, we quantified the fraction of RFP^+ cells within each population. Strikingly, HSCs exhibited unusually high autophagic activity at steady state (Fig. 1B,C). 74% of HSCs were RFP^+ as compared to 55% of MPPs, 23% of CMPs, 31 of GMPs, and 8% of MEPs. In addition, RFP fluorescence intensity was much higher in HSCs compared to all progenitor populations (Fig. 1C), suggesting that autophagic HSCs have more autophagic vesicles than progenitors.

Since LC3 can be cytoplasmic, we confirmed that RFP expression faithfully reflected the presence of autophagosomes. Cytoplasmic and autophagosomal LC3 can be distinguished using microscopy based on diffuse and punctate expression, respectively[28,29]. 100% of RFP^+ HSCs and MPPs contained RFP^+ puncta when examined by confocal microscopy (Fig. 1D), validating that RFP^+ HSCs and MPPs contain autophagosomes.

CAG-RFP-EGFP-LC3 mice enable quantification of autophagic flux[27]. EGFP fluorescence is pH sensitive and quenched within acidic lysosomes[27]. Consequently, RFP^+EGFP^+ cells are enriched with early autophagic vesicles (autophagosomes), while RFP^+EGFP^- cells contain late autophagic vesicles (autolysosomes), and RFP^-EGFP^- cells contain no detectable autophagic vesicles (Fig. 1E). Based on these parameters, RFP^+EGFP^+ cells have low autophagic flux, RFP^+EGFP^- cells have high autophagic flux, and RFP^-EGFP^- cells have no detectable autophagic flux[27]. We implemented a conservative gating strategy that was validated by confocal microscopy to resolve RFP^+EGFP^+, RFP^+EGFP^-, and RFP^-EGFP^- populations by flow cytometry (Fig. 1E,F, S1C,D). We confirmed that based on this gating, sorted RFP^+EGFP^+, RFP^+EGFP^-, and RFP^-EGFP^- HSCs and MPPs exclusively contained RFP^+EGFP^+ puncta, RFP^+EGFP^- puncta, and no fluorescence, respectively (Fig. 1D). We then adopted this gating strategy to quantify autophagic flux within HSCs and progenitors in vivo by flow cytometry (Fig. 1E,F, S1A,B).

The majority of autophagic RFP^+ HSCs, and 45% of HSCs overall, exhibited high autophagic flux at steady state (Fig. 1G). In contrast, only 27% of MPPs, 9% of CMPs, 7% of GMPs, 3% of MEPs, and 6% of CLPs exhibited high autophagic flux (Fig. 1G, S1B). There also tended to be a greater fraction of HSCs with low autophagic flux compared to progenitors (Fig. 1H). Only 25% of HSCs exhibited undetectable autophagic flux, which was significantly less than all progenitor populations (Fig. 1I, S1B). We validated this quantification by sorting unfractionated HSCs from CAG-RFP-EGFP-LC3 mice and assessing RFP and EGFP expression by confocal microscopy. Using this unbiased approach, we determined that 41% of HSCs contained RFP^+EGFP^- puncta, 25% contained RFP^+EGFP^+ puncta, and 34% contained no puncta (Fig. S1E) which was similar to flow cytometric analysis.

To further confirm that HSCs exhibited more autophagy than progenitors in vivo, we assessed autophagic activity by quantifying p62 (*Sqstm1*[30]). p62 is an autophagosomal cargo protein degraded by autophagy, and thus lower p62 is indicative of elevated autophagy[29]. Consistent, with CAG-RFP-EGFP-LC3 mice, HSCs contained significantly less p62 than progenitors (Fig. S1F). To confirm that lower p62 was due to elevated autophagy and not to baseline differences in p62 expression, we conditionally deleted the essential autophagy gene *Atg5*[31] in the hematopoietic system of young adult *Mx1-Cre*;$Atg5^{fl/fl}$ ($Atg5^{-/-}$) mice. $Atg5^{-/-}$ HSCs and MPPs, but not restricted progenitors, exhibited a significant increase in p62 abundance compared to controls (Fig. S1G), indicating that autophagy is readily ongoing within HSCs and MPPs at steady state. $Atg5^{-/-}$ HSCs exhibited similar p62 abundance compared to most restricted progenitors (Fig. S1G), indicating that baseline p62 expression is similar amongst HSCs and progenitors. Overall, data from orthogonal approaches indicate that most HSCs exhibit high autophagic activity at steady state in vivo, whereas autophagy declines in MPPs and is mostly absent in restricted myeloid progenitors.

Since autophagy is often associated with nutrient deprivation and quiescence, we wondered if activating HSCs would suppress autophagy and enhance proteasome activity. We treated young adult mice with cyclophosphamide and granulocyte colony-stimulating factor (GCSF). This treatment drives HSCs to modestly increase protein synthesis[10] and undergo rapid self-renewing divisions[32]. Strikingly, this proliferative stress further increased autophagy in HSCs, but did not significantly affect proteasome activity (Fig. S1H,I). These data support the conclusion that autophagy is the primary protein degradation pathway utilized by young adult HSCs under steady state and stress conditions in vivo.

HSCs transit between autophagic states

Deletion of key autophagy genes impairs HSC function[22,23,33,34]. In agreement with these studies, conditional deletion of *Atg5* in the hematopoietic system of young adult mice impaired HSC reconstituting activity and self-renewal potential (Fig. S2A-N). However, together with our quantitative assessment of autophagic flux, these data raised a key question: if autophagy promotes HSC function, do differences in steady state autophagic activity reflect functional heterogeneity amongst $CD150^{+}CD48^{-}$LSK cells?

To test this, we competitively transplanted 25 $RFP^{+}EGFP^{+}$, $RFP^{+}EGFP^{-}$ or $RFP^{-}EGFP^{-}$ $CD150^{+}CD48^{-}$LSK cells with 3×10^{5} wildtype competitor bone marrow cells into lethally irradiated mice (Fig. 2A). There was no significant difference in peripheral blood or bone marrow cell chimerism in recipients of the three HSC subsets (Fig. 2B-E, S2O-R). Similarly, there was no significant difference in the frequency of donor-derived HSCs in recipient bone marrow 16 weeks after transplant (Fig. 2F). These data indicate that all autophagic subsets of $CD150^{+}CD48^{-}$LSK cells contain bona fide HSCs, and that autophagic state is not associated with differences in long-term multilineage reconstituting potential.

At this point, we sought to reconcile an apparent contradiction; if autophagy is required for HSC function, how can $RFP^{-}EGFP^{-}$ HSCs with no detectable autophagy have normal long-term multilineage reconstituting activity? To answer this, we assessed autophagic activity within donor-derived HSCs. Interestingly, HSCs were not fixed in their autophagic potential. Regardless of which HSC subset was transplanted, recipient mice exhibiting long-term multilineage reconstitution all contained a similar distribution of donor-derived low-flux $RFP^{+}EGFP^{+}$, high-flux $RFP^{+}EGFP^{-}$ and undetectable-flux $RFP^{-}EGFP^{-}$ HSCs in their bone marrow (Fig. 2G-I). These data suggest that autophagic activity does not distinguish functionally distinct or hierarchically related HSCs. Rather, the HSC autophagic state is plastic, and HSCs can dynamically transition between no-flux, low-flux, and high-flux autophagic states.

Autophagic HSCs exhibit increased quiescence

Plasticity between autophagic states could mask distinctions between low-flux $RFP^{+}EGFP^{+}$, high-flux $RFP^{+}EGFP^{-}$ or no-flux $RFP^{-}EGFP^{-}$ HSCs. To capture potential static differences between these HSC subsets, we performed RNA-sequencing. The transcriptomes of low-flux $RFP^{+}EGFP^{+}$ and high-flux $RFP^{+}EGFP^{-}$ HSCs were very similar, as only 20 genes were differentially expressed (Fig. 2J; >1.5-fold; Padj<0.05). In contrast, $RFP^{-}EGFP^{-}$ HSCs with no detectable autophagic flux were transcriptionally distinct from both subsets

of RFP$^+$ autophagic HSCs, marked by differential expression (>1.5-fold; Padj<0.05) of nearly 300 genes (Fig. 2J). Gene set enrichment analysis revealed RFP$^-$EGFP$^-$ HSCs exhibited significantly increased expression of metabolic and biosynthetic pathways (Fig. 2K). Consistent with this, RFP$^-$EGFP$^-$ HSCs were twice as likely to be in the cell cycle, as marked by expression of Ki67, compared to autophagic RFP$^+$ HSCs (Fig. 2L). There were no differences in apoptosis between RFP$^+$ and RFP$^-$EGFP$^-$ HSCs (Fig. S2S). These data indicate that autophagic RFP$^+$ HSCs exhibit increased quiescence, and RFP$^-$ HSCs without detectable autophagy are significantly more likely to be cycling.

Crosstalk between proteasome and autophagy maintains HSC proteostasis

In most cells, proteasomes serve as the primary site for destruction of misfolded proteins, while autophagy typically contributes to proteostasis maintenance in response to stress[35,36]. However, given the low proteasome and high autophagic activity in HSCs, we wondered what the relative contributions of these pathways were to proteostasis maintenance. We previously established assays to quantify misfolded and unfolded protein in HSCs and progenitors by quantifying polyubiquitinated protein and tetraphenylethene maleimide (TMI)[37] fluorescence by flow cytometry, respectively[3]. Using these tools, we evaluated misfolded and unfolded protein abundance in HSCs and progenitors from mice treated with the proteasome inhibitor bortezomib[38] as well as autophagy-deficient *Atg5*$^{-/-}$ mice (Fig. 3A). We confirmed that *Atg5* deletion disrupted autophagy and that bortezomib inhibited proteasome activity in *Atg5*$^{-/-}$ cells (Fig. S1G, S3A). Surprisingly, neither proteasome inhibition nor disabling autophagy significantly increased the abundance of either polyubiquitinated (misfolded) or unfolded proteins in HSCs or progenitors (Fig. 3B,C, S3B,C). However, when proteasome and autophagy were simultaneously inhibited by administering bortezomib to *Atg5*$^{-/-}$ mice, misfolded and unfolded protein abundance increased significantly in HSCs (Fig. 3B,C).

Disruption of HSC proteostasis by combined proteasome and autophagy inhibition was also transcriptionally evident. RNA-sequencing revealed that combined proteasome and autophagy inhibition induced significant upregulation of gene sets associated with UPR activation, but neither proteasome inhibition nor *Atg5*-deficiency had that effect on its own (Fig. 3D-F, Table S1).

Next, we investigated potential crosstalk between the proteasome and autophagy pathways. We administered bortezomib to CAG-RFP-EGFP-LC3 mice and found compensatory activation of autophagy. The frequencies of RFP$^+$ HSCs and progenitors were significantly increased in response to proteasome inhibition (Fig. 3G,H). To confirm this was not due to decreased LC3 turnover by the proteasome[39], we determined that p62 abundance decreased in HSCs after bortezomib treatment (Fig. S3D), supporting the finding that autophagic activity is enhanced upon proteasome inhibition. We also quantified proteasome activity in HSCs and progenitors in *Atg5*$^{-/-}$ and control mice. Proteasome activity was significantly increased in *Atg5*$^{-/-}$ CD48$^-$LSK HSCs/MPPs compared to controls (Fig. 3I). In contrast, restricted progenitors, which have low autophagic activity at steady state, exhibited no compensatory increase in proteasome activity when autophagy was disabled (Fig. 3J). These data indicate that similar to other cells[40,41], HSCs and progenitors can activate autophagy

in response to proteasome inhibition. However, only HSCs and MPPs that have high steady state autophagic activity, trigger compensatory increases in proteasome activity in response to autophagy disruption. Overall, these data demonstrate that HSCs can utilize bidirectional compensatory crosstalk between proteasome and autophagy to prevent the accumulation of misfolded and unfolded proteins.

HSC aging is associated with reduced autophagic flux and increased proteasome activity

The finding that young adult HSCs exhibit high autophagic activity at steady state, along with previous reports that autophagy becomes disrupted in HSCs during aging[24], prompted us to examine protein degradation activity within old adult (22–24 month-old) HSCs. Although the frequency of cells undergoing autophagy was unchanged between young and old HSCs (Fig. S3F), there was a significant age-associated decrease in the frequency of high flux $RFP^{+}EGFP^{-}$ HSCs from 45% to 19% and a concomitant increase in low flux $RFP^{+}EGFP^{+}$ HSCs from 13% to 29% (Fig. 3K, S3E). These data indicate that autophagic flux declines in HSCs during aging. Interestingly, the reduction in autophagic flux was opposed by increased proteasome activity (Fig. 3L), mirroring the crosstalk observed within young adult HSCs when autophagy was disrupted (Fig. 3G,I). These data suggest that crosstalk between protein degradation systems is physiologically operative during HSC aging, and that HSC aging is associated with a shift in protein degradation characterized by diminished autophagic flux and heightened proteasome activity.

HSCs preferentially traffic misfolded proteins to aggresomes in a Bag3-dependent manner

We next simultaneously inhibited proteasome activity and autophagy by administering bortezomib to $Atg5^{-/-}$ mice and performed RNA-sequencing on HSCs. Combined proteasome and autophagy inhibition induced widespread transcriptional changes, with significant changes (>1.5-fold; Padj<0.05) in 1386 genes compared to vehicle treated wildtype controls (Fig. 4A). One of the most significantly upregulated genes was *Hspb8* (Fig. 4A,B). *Hspb8* encodes the small heat shock protein B8, which is a member of the Bag3-Hspb8-Hsp70-CHIP complex, which promotes trafficking of damaged and misfolded proteins to aggresomes[42,43]. Aggresomes are perinuclear inclusion bodies in which misfolded and aggregated proteins are concentrated and sequestered in a cage of intermediate filaments (e.g. vimentin), and are typically substrates for a selective form of autophagy (aggrephagy)[44]. The Bag3 complex is opposed by the Bag1 complex, which promotes substrate delivery to proteasomes (Fig. 4C)[45]. Bag3 competes with Bag1 for Hsp70 bound clients, and thus the ratio of Bag3 to Bag1 can dictate the destination of misfolded proteins[42,45]. Similar to *Hspb8*, *Bag3* expression was significantly increased in HSCs from $Atg5^{-/-}$ mice treated with bortezomib, but *Bag1* expression was unchanged (Fig. S4A,B). This resulted in a significant increase in the *Bag3* to *Bag1* ratio (Fig. 4D). These data suggest that in the absence of proteasome and autophagy function, HSCs may increasingly direct misfolded proteins to aggresomes.

Aggresomes have been reported to form specifically under stress conditions, such as when the proteasome is overwhelmed. Given their low proteasome activity, we wondered if HSCs might form aggresomes at steady state. We mined previous RNA-sequencing data comparing mouse and human HSCs and restricted progenitors[16,26,46].

Strikingly, HSCs expressed significantly more *Hspb8* than other hematopoietic cell populations (Fig. 4E). In fact, *Hspb8* was minimally or not expressed by most other hematopoietic cells and was specifically expressed by HSCs. Furthermore, HSCs expressed a 2–3-fold higher ratio of *Bag3* to *Bag1* than each of the other progenitor populations (Fig. 4F). Similarly, cord blood-derived human HSCs ($Lin^-CD34^+CD38^-CD45RA^-CD90^+CD49f^+$) express significantly more *BAG3* and a higher ratio of *BAG3* to *BAG1* than CMPs ($Lin^-CD34^+CD38^+CD10^-CD7^-CD45RA^-CD135^+$) and GMPs ($LinCD34^+CD38^+CD10^-CD7^-CD45RA^+$)[26,46] (Fig. 4G, S4C, D). These data suggest that at steady state, mouse and human HSCs may preferentially traffic misfolded proteins to aggresomes.

We used confocal microscopy to quantify the frequency of aggresome-containing HSCs. Aggresomes are identified based on co-localization of protein aggregates (detected using ProteoStat, a fluorescent rotor molecule that binds protein aggregates)[47] with vimentin[35,48]. Strikingly, ~68% of young adult HSCs contained aggresomes in vivo, which was significantly higher than restricted myeloid progenitors (Fig. 4H, I). To test if aggresome formation in HSCs is dependent on Bag3, we conditionally deleted *Bag3* in young adult *Mx1-Cre*;$Bag3^{fl/fl}$ ($Bag3^{-/-}$) mice. *Bag3* deletion significantly reduced the frequency of HSCs with aggresomes from 68% to 17% (Fig. 4J, K). These data indicate that young adult HSCs readily and preferentially form aggresomes at steady state in vivo in a Bag3-dependent manner.

HSCs preferentially depend on autophagy to maintain proteostasis by degrading protein aggregates

Aggresome formation is thought to be cytoprotective by locally concentrating protein aggregates and preventing their dissemination throughout the cell[44]. While protein aggregates can be degraded either by proteasomes or chaperone-mediated autophagy (preferentially active in HSCs[23]), they must first be selectively degraded into soluble single peptides via macroautophagy in a process referred to as aggrephagy[49]. The accumulation of misfolded/aggregated proteins in aggresomes thus serves to facilitate their clearance[13,49]. Since HSCs preferentially form aggresomes, we hypothesized that they might depend upon aggrephagy to prevent the widespread accumulation of protein aggregates.

To test this, we assessed the impact of *Bag3*- and *Atg5*-deficiency on protein aggregate levels in HSCs by quantifying ProteoStat fluorescence. The decline in aggresome formation in $Bag3^{-/-}$ HSCs was associated with a significant ~1.8-fold accumulation of protein aggregates (Fig. 4L). Disabling autophagy similarly resulted in protein aggregate accumulation within $Atg5^{-/-}$ HSCs, but not restricted progenitors (Fig. S4H). In contrast, proteasome inhibition had no effect on protein aggregate abundance in HSCs or progenitors (Fig. S4I). While $Bag3^{-/-}$ HSCs did not exhibit overall changes in proteasome activity, they became increasingly reliant on the proteasome to maintain proteostasis. Bortezomib treatment significantly increased polyubiquitinated protein in $Bag3^{-/-}$ HSCs but not in wildtype controls or $Bag3^{-/-}$ progenitors that had relatively normal levels of misfolded/unfolded protein (Fig. S4E,F), which is reminiscent of effects of bortezomib on $Atg5^{-/-}$

HSCs (Fig. 3B,C). These data demonstrate that HSCs specifically depend on aggrephagy to eliminate protein aggregates and maintain proteostasis.

Bag3$^{-/-}$ HSCs are myeloid-biased and have diminished self-renewal activity

To determine whether Bag3-mediated aggrephagy supports HSC function, we competitively transplanted 25 wildtype or *Bag3*$^{-/-}$ HSCs into irradiated recipients. Although donor B and T cell reconstitution were similar between wildtype and *Bag3*$^{-/-}$ HSCs (Fig. 4M-O), myeloid chimerism was significantly elevated in recipients of *Bag3*$^{-/-}$ HSCs (Fig. 4P). Analysis of lineage distribution of donor-derived cells in the bone marrow of transplant recipients confirmed that *Bag3*$^{-/-}$ HSCs have a significant myeloid bias (Fig. 4Q). We observed a >50% reduction in relative B cell chimerism and >60% increase in relative myeloid cell chimerism from *Bag3*$^{-/-}$ compared to wildtype HSCs. Moreover, *Bag3*$^{-/-}$ HSCs exhibited reduced long-term multilineage reconstituting potential upon serial transplantation. A substantially smaller fraction of secondary recipients of *Bag3*$^{-/-}$ HSCs exhibited long-term multilineage reconstitution compared to controls (Fig. 4R, S4J-M). Consistent with these data, old adult (22–25 month-old) *Bag3*$^{-/-}$ mice exhibited a ~4-fold reduction in HSC frequency and number (Fig. 4S, T), as well as significant myeloerythroid expansion in the spleen at the expense of B lineage cells (Fig. S4N). Overall, these data reveal that Bag3-mediated aggresome formation is critical to sustaining balanced differentiation and normal self-renewal capacity of HSCs.

Aging is associated with a loss of aggresomes in HSCs

The myeloid-biased differentiation and diminished self-renewal of *Bag3*$^{-/-}$ HSCs is reminiscent of changes that occur in HSCs during aging[50]. Furthermore, loss of proteostasis is a hallmark of aging[51], and recent studies suggest that aging HSCs experience proteotoxic stress[4]. Consequently, we examined aggresomes in old adult HSCs. While most young adult HSCs contained aggresomes, old adult HSCs almost completely lacked aggresomes (Fig. 4U, V). The age-related loss of aggresomes was restricted to the HSC compartment, as aggresomes were present in young and old adult myeloid progenitors at similar frequencies (Fig. 4V). Loss of aggresomes in HSCs did not appear to be caused by changes in expression of *Bag1* or *Bag3* complex constituents (Fig. S4O), suggesting that other yet unidentified changes disrupt aggresomes in aging HSCs. Overall, these results reveal that HSCs exhibit fundamental changes in proteostasis regulation during aging, and suggest that aggresome loss and aggrephagy dysfunction contribute to age-related declines in HSC fitness.

DISCUSSION

Though the ubiquitin proteasome system is considered the canonical degradation pathway for misfolded proteins[36], we found that HSCs preferentially depend on aggrephagy to maintain proteostasis in vivo. We identified Bag3 as a regulator of HSC proteostasis responsible for trafficking misfolded proteins to aggresomes and promoting aggrephagy. Autophagy is highly active within HSCs but not restricted progenitors at steady state in vivo (Fig. 1). Prior studies reported a role for autophagy in promoting HSC function, but this was largely attributed to its bulk degradative activity[22,25,33,52]. Recent studies have begun to uncover critical selective forms of autophagy that are preferentially important for HSCs[23,24].

Here, we found that HSCs preferentially depend on aggrephagy to selectively eliminate aggregated proteins and maintain proteostasis, and that disruptions in proteostasis partly contribute to HSC defects associated with impaired autophagy.

Mouse and human HSCs preferentially express components of the Bag3 complex (Fig. 3), which promotes trafficking of misfolded/unfolded proteins to aggresomes[43] and chaperone assisted selective autophagy[53]. Why do HSCs preferentially traffic misfolded proteins to aggresomes and utilize aggrephagy to maintain proteostasis? One possibility is that it enables finer control over resource allocation. Degrading misfolded proteins via the proteasome results in immediate recycling of amino acids into the cytoplasmic pool[54] that can be used for de novo protein synthesis. This may be preferred by rapidly dividing progenitors in constant need of amino acids to support high protein biogenesis demands, but may be suboptimal for HSCs that depend on lower protein synthesis rates[3,4,10,16,55,56]. In contrast, storing misfolded proteins in aggresomes or autophagosomes in quiescent cells preserves raw materials for when they are most needed, such as in response to proliferative or regenerative cues. It also provides a cell intrinsic cache of resources that could make HSCs less reliant on importing amino acids and thus less sensitive to fluctuations in nutrient availability. In support of this model, lysosomal biogenesis is associated with HSC quiescence and HSC cycling is associated with lysosomal activation[57,58], which is required for degradation of protein aggregates. A similar phenomenon of aggregate degradation supports neural stem cell activation[15,59]. In addition, HSCs that asymmetrically inherit more autophagosomes are more likely to preserve their stemness[60].

Disrupting aggresome assembly in *Bag3*$^{-/-}$ HSCs leads to myeloid-biased differentiation and diminished self-renewal (Fig. 4), which are two phenotypes associated with HSC aging. Declines in self-renewal were evident as *Bag3*$^{-/-}$ HSCs exhibited diminished serial long-term multilineage reconstituting activity. Interestingly, there was a bimodal effect in secondary transplants, as a substantial fraction of recipients of *Bag3*$^{-/-}$ HSCs failed to exhibit long-term multilineage reconstitution while others exhibited robust reconstitution (this effect was spread across multiple donors and experiments; Fig. S4J-M). One possible explanation is that *Bag3*-deficiency exerts a selective pressure that supports the emergence of an HSC subset that tolerates aggresome loss, perhaps through activation of proteotoxic stress response pathways. Consistent with this idea, aggresomes are mostly lost in old adult HSCs (Fig. 4), and aging HSCs activate the heat shock response[4,61], a key proteotoxic stress response pathway that promotes HSC fitness. Together, these data raise the possibility that aggresome loss and proteostasis dysfunction apply critical selective pressures that contribute to age-related changes in HSC fitness and function.

Aging is associated with proteasome dysfunction in multiple tissues, including the brain, and compensatory activation of autophagy is critical for preventing accumulation of protein aggregates associated with age-related neurodegenerative disorders[62]. Interestingly, this phenomenon is reversed within HSCs, which exhibit age-related declines in autophagic flux and compensate by increasing proteasome activity during aging. Future studies uncovering the mechanism of age-related proteasome activation in HSCs could offer important insights for ameliorating proteostasis dysfunction in other tissues and cell types.

Bidirectional crosstalk between the ubiquitin proteasome system and autophagy in HSCs may also have important therapeutic implications in cancer. Proteasome inhibitors are widely used to treat multiple myeloma, and their effectiveness partly depends on proteostasis disruption and UPR activation[63,64]. However, proteasome inhibitors are largely ineffective in treating other cancers[65]. Similarly, drugs that inhibit autophagy have been largely ineffective as cancer therapeutics[66]. Compensatory increases in autophagy in response to proteasome inhibition and increased proteasome activity in response to autophagy inhibition may contribute to the ineffectiveness of these therapies. Dual inhibition of these pathways or targeting potential mechanisms that contribute to this crosstalk may yield improved outcomes for cancer patients.

LIMITATIONS OF THE STUDY

Our study uncovers key differences in HSC proteostasis regulation by the proteasome and autophagy. One limitation of this comparison is that autophagy disruption was examined via genetic intervention (*Atg5*$^{-/-}$), while proteasome disruption was examined acutely in response to pharmacological inhibition.

Our data indicate that the HSC autophagic state is plastic, and that HSCs can transition between high, low, and no autophagic flux states after transplantation (Fig. 2). However, to what extent this occurs at steady state remains unknown. Furthermore, transplantation reduces autophagic activity in HSCs. At steady state, ~75% of HSCs exhibit ongoing autophagy (Fig. 1), but after transplantation that number is reduced to ~50% (Fig. 2). Similarly, autophagic flux is reduced in HSCs during aging (Fig. 3). It remains unclear how these prolonged and chronic stressors dysregulate autophagy. Elucidating how and why autophagic activity changes in HSCs could reveal strategies to preserve or enhance autophagy to improve HSC proteostasis, fitness, and longevity.

While aggresome formation depends upon Bag3 in young adult HSCs, it does not appear that changes in expression of Bag3 complex members underly declines in aggresomes in old adult HSCs. The mechanism underlying the age-related loss of aggresomes in HSCs is a limitation that should be addressed in future studies. One possibility is that since aggresome formation is microtubule-dependent [44], old adult HSCs may be unable to support aggresome assembly as a consequence of their loss of tubulin polarization[67]. Uncovering mechanisms of aggresome dysfunction could have important implications for rejuvenating aged HSCs.

STAR METHODS

RESOURCE AVAILABILITY

LEAD CONTACT—Further information and requests for resources and reagents should be directed to and will be fulfilled by the lead contact, Dr. Robert Signer (rsigner@ucsd.edu).

MATERIALS AVAILABILITY—This study did not generate new unique reagents.

DATA AND CODE AVAILABILITY—RNA-seq data have been deposited at GEO and are publicly available as of the date of publication. Accession numbers are listed in the

key resources table. This paper does not report original code. Any additional information required to reanalyze the data reported in this paper is available from the lead contact upon request.

EXPERIMENTAL MODEL AND SUBJECT DETAILS

Mice.—*Mx1-Cre* [68], *Atg5*^{fl} [31], *Bag3*^{fl} [69], and CAG-RFP-EGFP-LC3 [27] mice have been previously described. Mice were all backcrossed for at least ten generations onto a C57BL background. To generate *Mx1-Cre*$^{+}$;*Atg5*$^{fl/fl}$ mice we intercrossed *Mx1-Cre* and *Atg5*$^{fl/fl}$ mice. Once generated, *Mx1-Cre*$^{+}$;*Atg5*$^{fl/fl}$ mice were bred with *Atg5*$^{fl/fl}$ mice to maintain the colony. To generate *Mx1-Cre*$^{+}$;*Bag3*$^{fl/fl}$ mice we intercrossed *Mx1-Cre* and *Bag3*$^{fl/fl}$ mice. Once generated, *Mx1-Cre*$^{+}$;*Bag3*$^{fl/fl}$ mice were bred with *Bag3*$^{fl/fl}$ mice to maintain the colony. CAG-RFP-EGFP-LC3 mice were maintained by breeding CAG-RFP-EGFP-LC3$^{Tg/+}$ mice with C57BL6/J mice. C57BL6/J were used throughout the study. C57BL6.SJL (CD45.1) mice were used in transplantation experiments. Both male and female mice between 6 and 12 weeks (young adult) or 22–25 months (old adult) of age were used in these studies. All mice were housed in the vivarium at the UC San Diego Moores Cancer Center in specific pathogen-free conditions. All protocols were approved by the UC San Diego Institutional Animal Care and Use Committee.

METHOD DETAILS

PIPC treatment.

Expression of *Mx1-Cre* was induced by three injections of 10 mg PIPC administered intraperitoneally every other day to 6-week-old mice. Subsequent analyses were performed at least 7 days after the final PIPC injection.

Cyclophosphamide and GCSF treatment.

Mice were injected with 4 mg of cyclophosphamide intraperitoneally followed by two daily subcutaneous injections of 5 μg of GCSF. Mice were analyzed one day after the final GCSF injection.

Flow cytometry and cell sorting.

For flow cytometric analysis and isolation of specific hematopoietic progenitors, cells were incubated with combinations of antibodies to the following cell-surface markers, conjugated to FITC, PE, PerCP-Cy5.5, APC, PE-Cy7, Alexa Fluor 700, APC-eFluor 780, or biotin (antibody clones are given in brackets in the following list): CD3ε (17A2), CD4 (GK1.5), CD5 (53–7.3), CD8a (53–6.7), CD11b (M1/70), CD16/32 (FcgRII/III; 93), CD34 (RAM34), CD43 (R2/60), CD45.1 (A20), CD45.2 (104), CD45R (B220; RA3–6B2), CD48 (HM48–1), CD71 (R17217), CD117 (cKit; 2B8), CD127 (IL7Ra; A7R34), CD150 (TC15–12F12.2), Ter119 (TER-119), Sca-1 (D7, E13–161.7), Gr-1 (RB6–8C5), IgM (II/41), and CD135 (A2F10). For isolation of HSCs and MPPs, Lineage markers included CD3, CD5, CD8, B220, Gr-1 and Ter119. For isolation of CMPs, GMPs and MEPs, these Lineage markers were supplemented with additional antibodies against CD4 and CD11b. Biotinylated antibodies were visualized by incubation with PE-Cy7 conjugated streptavidin.

All reagents were acquired from eBiosciences, or BioLegend. All incubations were for 30–90 min on ice.

HSCs, MPPs, $CD34^{+}CD16/32^{low}CD127^{-}Lineage^{-}Sca\text{-}1^{-}c\text{-}kit^{+}$ CMPs[70], $CD34^{+}CD16/32^{high}CD127^{-}Lineage^{-}Sca\text{-}1^{-}c\text{-}kit^{+}$ GMPs[19], $CD34^{-}CD16/32^{-/low}CD127^{-}Lineage^{-}Sca\text{-}1^{-}c\text{-}kit^{+}$ MEPs[19] were pre-enriched by selecting $c\text{-}kit^{+}$ cells using paramagnetic microbeads and an autoMACS magnetic separator (Miltenyi Biotec) before sorting. $CD127^{+}Flt3^{+}Lin^{-}Sca1^{low}cKit^{low}$ CLPs[71,72] were sorted directly. Non-viable cells were excluded from sorts and analyses using 4',6-diamidino-2-phenylindole (DAPI).

Cell sorting was performed on BD FACSAria I and BD FACSAria II, or BD FACSAria Fusion. Flow cytometry samples were acquired using a BD LSR I, BD LSR II, or BD FACSymphony A1. Data were analyzed using FlowJo (TreeStar) software.

Proteasome inhibition.

Mice were administered 10mg/kg of bortezomib (Cell Signaling) diluted in 10% (v/v) DMSO retro-orbitally 48 hours and 24 hours before analysis.

Transplantation assays.

For bone marrow transplants, 5×10^{5} donor ($CD45.2^{+}$) bone marrow cells were competitively transplanted with 5×10^{5} ($CD45.1^{+}$) whole bone marrow cells into lethally irradiated congenic recipients ($CD45.1^{+}$). For HSC transplants, 25 donor HSCs ($CD45.2^{+}$) were competitively transplanted with 3×10^{5} whole bone marrow cells ($CD45.1^{+}$) into lethally irradiated congenic recipients ($CD45.1^{+}$). A Mark I Cesium source irradiator (J.L. Shepherd) was used to deliver two doses of 550 rad 4 hours apart for a total lethal dose of 1,100 rad.

Peripheral blood from tail veins of recipient mice was collected every 4 weeks for a total of 16 weeks. Red blood cells were lysed with ammonium chloride potassium buffer. Cells were stained with antibodies against CD45.2, CD45.1, CD45R (B220), CD11b, CD3, and Gr-1 to evaluate donor cell engraftment. Sixteen weeks post-transplant, bone marrow was analyzed for HSC engraftment and multilineage chimerism.

For secondary transplants, 3×10^{6} bone marrow cells collected from primary recipients were transplanted non-competitively into irradiated recipient mice. Primary recipients used for secondary transplantation had long-term multilineage reconstitution by donor cells and median levels of donor-cell reconstitution for the treatments from which they originated. Transplanted mice were administered drinking water with Baytril (250 mg/L) for the first 4 weeks posttransplant. Mice were considered long-term multilineage reconstituted if they exhibited >0.5% donor derived peripheral blood B, T and myeloid cells 16 weeks post-transplant.

Proteasome activity.

5,000–10,000 cells were isolated and transferred to solid opaque 96-well plates. Proteasome activity was measured using Proteasome-Glo Chymotrypsin-Like Cell-Based Assay (Promega). Luminescence was measured using Tecan Spark plate reader.

Confocal microscopy.

Unfractionated, RFP^+EGFP^-, RFP^+EGFP^+, and $RFP^-EGFP^-CD150^+CD48^-$LSK HSCs were FACS isolated from the bone marrow of CAG-RFP-EGFP-LC3 mice. Cells were fixed in 4% PFA (Electron Microscopy Sciences) for 10 min at room temperature before incubation with DAPI for 5 min. Cells were washed with PBS and then affixed onto coverslips coated with 0.1% poly-L-lysine (Sigma) diluted 1:5 in molecular biology grade water. Coverslips were mounted onto slides using ProLong Diamond Antifade Mountant (Fisher). Images were acquired on Zeiss LSM880 microscope equipped with Airyscan using a 63X objective. Images were processed with Zeiss ZEN blue/black software and analyzed using FIJI (ImageJ).

For aggresome staining, sorted cells were spun onto coated slides at 450 RPM for 5 min (Cytospin). Cells were then fixed in 4% paraformaldehyde in PBS for 15 min at room temperature. Cells were washed with PBS then permeabilized with PBS supplemented with 0.1% Triton X-100, 0.03% Tween 20 and 1% BSA for 20 min at room temperature. Cells were washed with PBS supplemented with 0.03% Tween 20. Cells were blocked with PBS supplemented with 1% BSA and 0.03% Tween 20 for 1 hour at room temperature. Samples were incubated with anti-vimentin antibody (Millipore AB5733, 1:1000) overnight at 4°C. Cells were washed and incubated with goat anti-chicken IgY Alexa Fluor 488 (Thermo A-11039, 1:500) and ProteoStat (Enzo, 1:5000) for 1 hour at room temperature. Cells were washed with PBS. Before the last wash, nuclei were stained with DAPI for 5 min at room temperature. Cells were mounted with ProLong Diamond Antifade Mountant (Fisher). Raw images were processed using ZEN Blue and maximum intensity projection of z-stacks was generated using FIJI. Blue (DAPI), green (vimentin), and red (ProteoStat) channels were merged and aggresome presence was determined based on co-localization of vimentin and ProteoStat structures. Cells were considered aggresome-positive if they exhibited co-localization of a vimentin cage with ProteoStat-positive puncta. Cells were considered aggresome-free if they did not exhibit co-localization.

Misfolded (polyubiquitinated) protein.

6×10^6 bone marrow cells were stained with cell surface markers to identify HSCs and progenitor populations. Cells were fixed in 1% PFA and permeabilized in saponin before incubation with 1:500 primary pan-ubiquitin antibody, clone FK2 (Sigma) followed by 1:500 goat anti-mouse IgG AF-488 secondary antibody (Thermo). Cells were analyzed by flow cytometry.

Unfolded protein.

6×10^6 bone marrow cells were stained with cell surface markers to identify HSCs and progenitor populations. Samples were washed twice in Ca^{2+}- and Mg^{2+}-free PBS. Tetraphenylethene maleimide[37] (TMI; stock 2 mM in DMSO) was diluted in PBS (50 mM final concentration) and added to each sample. Samples were incubated at 37°C for 45 min. Samples were washed twice in PBS and analyzed by flow cytometry. DAPI was omitted from these samples because of spectral overlap.

Aggregated protein.

2,000–5,000 HSCs or progenitors were isolated by FACS then fixed in 1% PFA followed by permeabilization with saponin. Samples were stained with ProteoStat (Enzo) (1:2500) for 30 min then resuspended in PBS with DAPI for flow cytometric analysis.

p62 staining.

6×10^6 bone marrow cells were stained with cell surface markers to identify HSCs and progenitor populations. Cells were fixed and permeabilized using BD Cytofix/Cytoperm solutions and washed with BD Perm/Wash buffer. Samples were incubated with anti-p62 antibody (ab194721) for 30 min at room temperature[73].

Annexin V staining.

6×10^6 bone marrow cells from CAG-RFP-EGFP-LC3 mice were stained with cell surface markers to identify HSCs. Annexin V Apoptosis Detection Kit APC (eBioscience) was used to detect Annexin V.

Cell cycle status.

For Ki67 analysis of autophagy subsets, approximately 2,000 RFP^-EGFP^- or RFP^+ $CD48^-LSK$ cells were FACS isolated from the bone marrow of CAG-RFP-EGFP-LC3 mice.

Cells were fixed and permeabilized as described above and stained with AlexaFluor 647 mouse anti-Ki67 (BD; Clone B56).

RNA-sequencing.

For RNA-sequencing analysis, total RNA was extracted from up to 10,000 HSCs using the RNeasy Plus Micro Kit (Qiagen). Illumina mRNA libraries were prepared using the SMARTseq2 protocol[74]. 2.6μl of total RNA was used in the SMARTSeq2 protocol (70pg to 1.62ng). 18 cycles of PCR were performed for the cDNA preamplification step and 12 cycles were performed for the tagmentation library preparation. The resulting libraries were pooled and deep sequenced on the Illumina NovaSeq using paired-end reads with both forward and reverse read lengths of 50 nucleotides (60–100M reads per condition). The reads that passed Illumina filters were filtered for reads aligning to tRNA, rRNA, adapter sequences, and spike-in controls. The reads were then aligned to the GRCm38 reference genome using STAR (v2.6.1)[75]. DUST scores were calculated with PRINSEQ Lite (v 0.20.3)[76] and low-complexity reads (DUST > 4) were removed from the BAM files. The alignment results were parsed via the SAMtools[77] to generate SAM files. Read counts to each genomic feature were obtained with the featureCounts program (v 1.6.5)[78] using the default options along with a minimum quality cut off (Phred > 10). After removing absent features (zero counts in all samples), the raw counts were then imported to Bioconductor package DESeq2 (v 1.24.0)[79] to identify differentially expressed genes among samples. P-values for differential expression are calculated using the Wald test for differences between the base means of two conditions. These P-values are then adjusted for multiple test correction using Benjamini Hochberg algorithm. We considered genes differentially

expressed between two groups of samples when the DESeq2 analysis resulted in an adjusted P-value of <0.05 and the difference in gene expression was at least 1.5-fold.

Gene set enrichment analysis was done using the “GseaPreranked” method with “classic” scoring scheme. MSigDB Gene sets were downloaded in GMT format for mouse using R package msigdbr v7.4.1. Rank files for each DE comparison of interest were generated by assigning a rank of negative log10(pValue) to genes with log2FoldChange greater than zero and a rank of positive log10(pValue) to genes with log2FoldChange less than zero

QUANTIFICATION AND STATISTICAL ANALYSIS

Group data are represented by mean ± standard deviation, except for transplantation data which are represented as mean ± standard error of the mean. The specific type of statistical test used for each figure panel is described in the figure legends. For t-tests, a confidence interval of 95% was used. For normalized data, means were calculated and statistical tests were performed using log10-transformed data and then means were back-transformed to prevent data skewing. No randomization or blinding was used in any experiments. The only mice excluded from any experiment were those that died after transplantation. We performed multiple independent experiments with multiple biological replicates to ensure the reproducibility of our findings.

Supplementary Material

Refer to Web version on PubMed Central for supplementary material.

ACKNOWLEDGMENTS

Work in the Signer Laboratory is supported by the NIH/NIDDK (R01DK116951; R01DK124775), NIH/NCI (U01CA267031), the Blood Cancer Discoveries Grant program (8025-20) through The Leukemia & Lymphoma Society, The Mark Foundation for Cancer Research and The Paul G. Allen Frontiers Group, the American Cancer Society (CSCC-RSG-23-994830-01-CSCC), the Sanford Stem Cell Institute, and the UC San Diego Moores Cancer Center which is supported by the NCI Cancer Center Support Grant (P30CA023100). The LJI and Moores Cancer Center Flow Cytometry and Microscopy core facilities are supported by the NIH Shared Instrumentation Grant Program (S10 RR027366, S10OD032316, S10OD021831). Some figures were generated using Biorender. We thank N. Mizushima, J. Chen, Y. Hong, J. Magee, K. Dorshkind, S. Morrison, and C. Jamieson for reagents and/or advice.

REFERENCES

1. Chua BA, Van Der Werf I, Jamieson C, and Signer RAJ (2020). Post-Transcriptional Regulation of Homeostatic, Stressed, and Malignant Stem Cells. Cell Stem Cell 26, 138–159. 10.1016/j.stem.2020.01.005. [PubMed: 32032524]
2. García-Prat L, Martínez-Vicente M, Perdiguero E, Ortet L, Rodríguez-Ubreva J, Rebollo E, Ruiz-Bonilla V, Gutarra S, Ballestar E, and Serrano AL (2016). Autophagy maintains stemness by preventing senescence. Nature 529, 37–42. [PubMed: 26738589]
3. Hidalgo San Jose L, Sunshine MJ, Dillingham CH, Chua BA, Kruta M, Hong Y, Hatters DM, and Signer RAJ (2020). Modest Declines in Proteome Quality Impair Hematopoietic Stem Cell Self-Renewal. Cell Rep 30, 69–80.e66. 10.1016/j.celrep.2019.12.003. [PubMed: 31914399]
4. Kruta M, Sunshine MJ, Chua BA, Fu Y, Chawla A, Dillingham CH, Hidalgo San Jose L, De Jong B, Zhou FJ, and Signer RAJ (2021). Hsf1 promotes hematopoietic stem cell fitness and proteostasis in response to ex vivo culture stress and aging. Cell Stem Cell 28, 1950–1965.e1956. 10.1016/j.stem.2021.07.009. [PubMed: 34388375]

5. Vilchez D, Simic MS, and Dillin A (2014). Proteostasis and aging of stem cells. Trends Cell Biol 24, 161–170. 10.1016/j.tcb.2013.09.002. [PubMed: 24094931]
6. Balch WE, Morimoto RI, Dillin A, and Kelly JW (2008). Adapting proteostasis for disease intervention. Science 319, 916–919. 10.1126/science.1141448. [PubMed: 18276881]
7. Blanco S, Bandiera R, Popis M, Hussain S, Lombard P, Aleksic J, Sajini A, Tanna H, Cortés-Garrido R, Gkatza N, et al. (2016). Stem cell function and stress response are controlled by protein synthesis. Nature 534, 335–340. 10.1038/nature18282. [PubMed: 27306184]
8. Llorens-Bobadilla E, Zhao S, Baser A, Saiz-Castro G, Zwadlo K, and Martin-Villalba A (2015). Single-Cell Transcriptomics Reveals a Population of Dormant Neural Stem Cells that Become Activated upon Brain Injury. Cell Stem Cell 17, 329–340. 10.1016/j.stem.2015.07.002. [PubMed: 26235341]
9. Sanchez Carlos G., Teixeira Felipe K., Czech B, Preall, Jonathan B, Zamparini, Andrea L, Seifert, Jessica RK, Malone, Colin D, Hannon, Gregory J, and Lehmann R (2016). Regulation of Ribosome Biogenesis and Protein Synthesis Controls Germline Stem Cell Differentiation. Cell Stem Cell 18, 276–290. 10.1016/j.stem.2015.11.004. [PubMed: 26669894]
10. Signer RA, Magee JA, Salic A, and Morrison SJ (2014). Haematopoietic stem cells require a highly regulated protein synthesis rate. Nature 509, 49–54. 10.1038/nature13035. [PubMed: 24670665]
11. Zismanov V, Chichkov V, Colangelo V, Jamet S, Wang S, Syme A, Koromilas, Antonis E, and Crist C (2016). Phosphorylation of eIF2α Is a Translational Control Mechanism Regulating Muscle Stem Cell Quiescence and Self-Renewal. Cell Stem Cell 18, 79–90. 10.1016/j.stem.2015.09.020. [PubMed: 26549106]
12. van Galen P., Kreso A., Mbong N., Kent DG., Fitzmaurice T., Chambers JE., Xie S., Laurenti E., Hermans K., Eppert K., et al. . (2014). The unfolded protein response governs integrity of the haematopoietic stem-cell pool during stress. Nature 510, 268272. 10.1038/nature13228.
13. Dikic I (2017). Proteasomal and Autophagic Degradation Systems. Annu Rev Biochem 86, 193–224. 10.1146/annurev-biochem-061516-044908. [PubMed: 28460188]
14. Vilchez D, Boyer L, Morantte I, Lutz M, Merkwirth C, Joyce D, Spencer B, Page L, Masliah E, Berggren WT, et al. (2012). Increased proteasome activity in human embryonic stem cells is regulated by PSMD11. Nature 489, 304–308. 10.1038/nature11468. [PubMed: 22972301]
15. Leeman DS, Hebestreit K, Ruetz T, Webb AE, McKay A, Pollina EA, Dulken BW, Zhao X, Yeo RW, Ho TT, et al. (2018). Lysosome activation clears aggregates and enhances quiescent neural stem cell activation during aging. Science 359, 1277–1283. 10.1126/science.aag3048. [PubMed: 29590078]
16. Signer RA, Qi L, Zhao Z, Thompson D, Sigova AA, Fan ZP, DeMartino GN, Young RA, Sonenberg N, and Morrison SJ (2016). The rate of protein synthesis in hematopoietic stem cells is limited partly by 4E-BPs. Genes Dev 30, 1698–1703. 10.1101/gad.282756.116. [PubMed: 27492367]
17. Kiel MJ, Yilmaz OH, Iwashita T, Yilmaz OH, Terhorst C, and Morrison SJ (2005). SLAM family receptors distinguish hematopoietic stem and progenitor cells and reveal endothelial niches for stem cells. Cell 121, 1109–1121. 10.1016/j.cell.2005.05.026. [PubMed: 15989959]
18. Challen GA, Pietras EM, Wallscheid NC, and Signer RAJ (2021). Simplified murine multipotent progenitor isolation scheme: Establishing a consensus approach for multipotent progenitor identification. Exp Hematol 104, 55–63. 10.1016/j.exphem.2021.09.007. [PubMed: 34648848]
19. Oguro H, Ding L, and Morrison SJ (2013). SLAM family markers resolve functionally distinct subpopulations of hematopoietic stem cells and multipotent progenitors. Cell Stem Cell 13, 102–116. 10.1016/j.stem.2013.05.014. [PubMed: 23827712]
20. Yang Z, and Klionsky DJ (2010). Mammalian autophagy: core molecular machinery and signaling regulation. Curr Opin Cell Biol 22, 124–131. 10.1016/j.ceb.2009.11.014. [PubMed: 20034776]
21. Murrow L, and Debnath J (2013). Autophagy as a stress-response and quality-control mechanism: implications for cell injury and human disease. Annu Rev Pathol 8, 105–137. 10.1146/annurev-pathol-020712-163918. [PubMed: 23072311]

22. Warr MR, Binnewies M, Flach J, Reynaud D, Garg T, Malhotra R, Debnath J, and Passegué E (2013). FOXO3A directs a protective autophagy program in haematopoietic stem cells. Nature 494, 323–327. 10.1038/nature11895. [PubMed: 23389440]
23. Dong S, Wang Q, Kao YR, Diaz A, Tasset I, Kaushik S, Thiruthuvanathan V, Zintiridou A, Nieves E, Dzieciatkowska M, et al. (2021). Chaperone-mediated autophagy sustains haematopoietic stem-cell function. Nature 591, 117–123. 10.1038/s41586-020-03129-z. [PubMed: 33442062]
24. Ho TT, Warr MR, Adelman ER, Lansinger OM, Flach J, Verovskaya EV, Figueroa ME, and Passegué E (2017). Autophagy maintains the metabolism and function of young and old stem cells. Nature 543, 205–210. 10.1038/nature21388. [PubMed: 28241143]
25. Mortensen M., Soilleux EJ., Djordjevic G., Tripp R., Lutteropp M., Sadighi-Aksh E., Stranks AJ., Glanville J., Knight S., Jacobsen SE., et al. . (2011). The autophagy protein Atg7 is essential for hematopoietic stem cell maintenance. J Exp Med 208, 455467. 10.1084/jem.20101145.
26. Xie SZ, Garcia-Prat L, Voisin V, Ferrari R, Gan OI, Wagenblast E, Kaufmann KB, Zeng AGX, Takayanagi SI, Patel I, et al. (2019). Sphingolipid Modulation Activates Proteostasis Programs to Govern Human Hematopoietic Stem Cell Self-Renewal. Cell Stem Cell 25, 639–653.e637. 10.1016/j.stem.2019.09.008. [PubMed: 31631013]
27. Li L, Wang ZV, Hill JA, and Lin F (2014). New autophagy reporter mice reveal dynamics of proximal tubular autophagy. J Am Soc Nephrol 25, 305–315. 10.1681/asn.2013040374. [PubMed: 24179166]
28. Kabeya Y, Mizushima N, Yamamoto A, Oshitani-Okamoto S, Ohsumi Y, and Yoshimori T (2004). LC3, GABARAP and GATE16 localize to autophagosomal membrane depending on form-II formation. J Cell Sci 117, 2805–2812. 10.1242/jcs.01131. [PubMed: 15169837]
29. Yoshii SR, and Mizushima N (2017). Monitoring and Measuring Autophagy. Int J Mol Sci *18*. 10.3390/ijms18091865.
30. Bjørkøy G, Lamark T, Pankiv S, Øvervatn A, Brech A, and Johansen T (2009). Monitoring autophagic degradation of p62/SQSTM1. Methods Enzymol 452, 181–197. 10.1016/s0076-6879(08)03612-4. [PubMed: 19200883]
31. Hara T, Nakamura K, Matsui M, Yamamoto A, Nakahara Y, Suzuki-Migishima R, Yokoyama M, Mishima K, Saito I, Okano H, and Mizushima N (2006). Suppression of basal autophagy in neural cells causes neurodegenerative disease in mice. Nature 441, 885–889. 10.1038/nature04724. [PubMed: 16625204]
32. Morrison SJ, Wright DE, and Weissman IL (1997). Cyclophosphamide/granulocyte colony-stimulating factor induces hematopoietic stem cells to proliferate prior to mobilization. Proc Natl Acad Sci U S A 94, 1908–1913. 10.1073/pnas.94.5.1908. [PubMed: 9050878]
33. Liu F, Lee JY, Wei H, Tanabe O, Engel JD, Morrison SJ, and Guan JL (2010). FIP200 is required for the cell-autonomous maintenance of fetal hematopoietic stem cells. Blood 116, 4806–4814. 10.1182/blood-2010-06-288589. [PubMed: 20716775]
34. Nomura N, Ito C, Ooshio T, Tadokoro Y, Kohno S, Ueno M, Kobayashi M, Kasahara A, Takase Y, Kurayoshi K, et al. (2021). Essential role of autophagy in protecting neonatal haematopoietic stem cells from oxidative stress in a p62independent manner. Scientific Reports 11, 1666. 10.1038/s41598-021-81076-z. [PubMed: 33462315]
35. Johnston JA, Ward CL, and Kopito RR (1998). Aggresomes: a cellular response to misfolded proteins. J Cell Biol 143, 1883–1898. 10.1083/jcb.143.7.1883. [PubMed: 9864362]
36. Rock KL, Gramm C, Rothstein L, Clark K, Stein R, Dick L, Hwang D, and Goldberg AL (1994). Inhibitors of the proteasome block the degradation of most cell proteins and the generation of peptides presented on MHC class I molecules. Cell 78, 761–771. 10.1016/S0092-8674(94)90462-6. [PubMed: 8087844]
37. Chen MZ, Moily NS, Bridgford JL, Wood RJ, Radwan M, Smith TA, Song Z, Tang BZ, Tilley L, and Xu X (2017). A thiol probe for measuring unfolded protein load and proteostasis in cells. Nature communications 8, 1–11.
38. Chen D, Frezza M, Schmitt S, Kanwar J, and Dou QP (2011). Bortezomib as the first proteasome inhibitor anticancer drug: current status and future perspectives. Curr Cancer Drug Targets 11, 239–253. 10.2174/156800911794519752. [PubMed: 21247388]

39. Jia R, and Bonifacino JS (2020). Regulation of LC3B levels by ubiquitination and proteasomal degradation. Autophagy 16, 382–384. 10.1080/15548627.2019.1709766. [PubMed: 31880195]
40. Tannous P, Zhu H, Nemchenko A, Berry JM, Johnstone JL, Shelton JM, Miller FJ Jr., Rothermel BA, and Hill JA (2008). Intracellular protein aggregation is a proximal trigger of cardiomyocyte autophagy. Circulation 117, 3070–3078. 10.1161/circulationaha.107.763870. [PubMed: 18541737]
41. Wang XJ., Yu J., Wong SH., Cheng AS., Chan FK., Ng SS., Cho CH., Sung JJ., and Wu WK. (2013). A novel crosstalk between two major protein degradation systems: regulation of proteasomal activity by autophagy. Autophagy 9, 1500–1508. 10.4161/auto.25573. [PubMed: 23934082]
42. Carra S, Seguin SJ, and Landry J (2008). HspB8 and Bag3: a new chaperone complex targeting misfolded proteins to macroautophagy. Autophagy 4, 237–239. 10.4161/auto.5407. [PubMed: 18094623]
43. Gamerdinger M, Kaya AM, Wolfrum U, Clement AM, and Behl C (2011). BAG3 mediates chaperone-based aggresome-targeting and selective autophagy of misfolded proteins. EMBO Rep 12, 149–156. 10.1038/embor.2010.203. [PubMed: 21252941]
44. Kopito RR (2000). Aggresomes, inclusion bodies and protein aggregation. Trends Cell Biol 10, 524–530. 10.1016/s0962-8924(00)01852-3. [PubMed: 11121744]
45. Gamerdinger M, Hajieva P, Kaya AM, Wolfrum U, Hartl FU, and Behl C (2009). Protein quality control during aging involves recruitment of the macroautophagy pathway by BAG3. Embo j 28, 889–901. 10.1038/emboj.2009.29. [PubMed: 19229298]
46. Laurenti E, Doulatov S, Zandi S, Plumb I, Chen J, April C, Fan JB, and Dick JE (2013). The transcriptional architecture of early human hematopoiesis identifies multilevel control of lymphoid commitment. Nat Immunol 14, 756–763. 10.1038/ni.2615. [PubMed: 23708252]
47. Navarro S, and Ventura S (2014). Fluorescent dye ProteoStat to detect and discriminate intracellular amyloid-like aggregates in Escherichia coli. Biotechnol J 9, 1259–1266. 10.1002/biot.201400291. [PubMed: 25112199]
48. Rock KL, Gramm C, Rothstein L, Clark K, Stein R, Dick L, Hwang D, and Goldberg AL (1994). Inhibitors of the proteasome block the degradation of most cell proteins and the generation of peptides presented on MHC class I molecules. Cell 78, 761–771. 10.1016/s0092-8674(94)90462-6. [PubMed: 8087844]
49. Lamark T, and Johansen T (2012). Aggrephagy: Selective Disposal of Protein Aggregates by Macroautophagy. International Journal of Cell Biology 2012, 736905. 10.1155/2012/736905.
50. Signer RA, and Morrison SJ (2013). Mechanisms that regulate stem cell aging and life span. Cell Stem Cell 12, 152–165. 10.1016/j.stem.2013.01.001. [PubMed: 23395443]
51. López-Otín C, Blasco MA, Partridge L, Serrano M, and Kroemer G (2013). The hallmarks of aging. Cell 153, 1194–1217. 10.1016/j.cell.2013.05.039. [PubMed: 23746838]
52. Nguyen-McCarty M, and Klein PS (2017). Autophagy is a signature of a signaling network that maintains hematopoietic stem cells. PLoS One 12, e0177054. 10.1371/journal.pone.0177054. [PubMed: 28486555]
53. Arndt V, Dick N, Tawo R, Dreiseidler M, Wenzel D, Hesse M, Fürst DO, Saftig P, Saint R, Fleischmann BK, et al. (2010). Chaperone-assisted selective autophagy is essential for muscle maintenance. Curr Biol 20, 143–148. 10.1016/j.cub.2009.11.022. [PubMed: 20060297]
54. Suraweera A, Münch C, Hanssum A, and Bertolotti A (2012). Failure of amino acid homeostasis causes cell death following proteasome inhibition. Mol Cell 48, 242–253. 10.1016/j.molcel.2012.08.003. [PubMed: 22959274]
55. Keyvani Chahi A, Belew MS, Xu J, Chen HTT, Rentas S, Voisin V, Krivdova G, Lechman E, Marhon SA, De Carvalho DD, et al. (2022). PLAG1 dampens protein synthesis to promote human hematopoietic stem cell self-renewal. Blood 140, 992–1008. 10.1182/blood.2021014698. [PubMed: 35639948]
56. Magee JA, and Signer RAJ (2021). Developmental Stage-Specific Changes in Protein Synthesis Differentially Sensitize Hematopoietic Stem Cells and Erythroid Progenitors to Impaired Ribosome Biogenesis. Stem Cell Reports 16, 20–28. 10.1016/j.stemcr.2020.11.017. [PubMed: 33440178]

57. García-Prat L., Kaufmann KB., Schneiter F., Voisin V., Murison A., Chen J., ChanSeng-Yue M., Gan OI., McLeod JL., Smith SA., et al. . (2021). TFEB-mediated endolysosomal activity controls human hematopoietic stem cell fate. Cell Stem Cell 28, 1838–1850.e1810. 10.1016/j.stem.2021.07.003. [PubMed: 34343492]
58. Liang R, Arif T, Kalmykova S, Kasianov A, Lin M, Menon V, Qiu J, Bernitz JM, Moore K, Lin F, et al. (2020). Restraining Lysosomal Activity Preserves Hematopoietic Stem Cell Quiescence and Potency. Cell Stem Cell 26, 359–376.e357. 10.1016/j.stem.2020.01.013. [PubMed: 32109377]
59. Morrow CS, Porter TJ, Xu N, Arndt ZP, Ako-Asare K, Heo HJ, Thompson EAN, and Moore DL (2020). Vimentin Coordinates Protein Turnover at the Aggresome during Neural Stem Cell Quiescence Exit. Cell Stem Cell 26, 558–568.e559. 10.1016/j.stem.2020.01.018. [PubMed: 32109376]
60. Loeffler D, Wehling A, Schneiter F, Zhang Y, Müller-Bötticher N, Hoppe PS, Hilsenbeck O, Kokkaliaris KD, Endele M, and Schroeder T (2019). Asymmetric lysosome inheritance predicts activation of haematopoietic stem cells. Nature 573, 426–429. 10.1038/s41586-019-1531-6. [PubMed: 31485073]
61. Chambers SM, Shaw CA, Gatza C, Fisk CJ, Donehower LA, and Goodell MA (2007). Aging hematopoietic stem cells decline in function and exhibit epigenetic dysregulation. PLoS Biol 5, e201. 10.1371/journal.pbio.0050201. [PubMed: 17676974]
62. Seidel K, Vinet J, Dunnen WF, Brunt ER, Meister M, Boncoraglio A, Zijlstra MP, Boddeke HW, Rüb U, Kampinga HH, and Carra S (2012). The HSPB8-BAG3 chaperone complex is upregulated in astrocytes in the human brain affected by protein aggregation diseases. Neuropathol Appl Neurobiol 38, 39–53. 10.1111/j.1365-2990.2011.01198.x. [PubMed: 21696420]
63. Lee A-H, Iwakoshi NN, Anderson KC, and Glimcher LH (2003). Proteasome inhibitors disrupt the unfolded protein response in myeloma cells. Proceedings of the National Academy of Sciences 100, 9946–9951. doi:10.1073/pnas.1334037100.
64. Obeng EA, Carlson LM, Gutman DM, Harrington WJ Jr., Lee KP, and Boise LH (2006). Proteasome inhibitors induce a terminal unfolded protein response in multiple myeloma cells. Blood 107, 4907–4916. 10.1182/blood-2005-08-3531. [PubMed: 16507771]
65. Manasanch EE, and Orlowski RZ (2017). Proteasome inhibitors in cancer therapy. Nature Reviews Clinical Oncology 14, 417–433. 10.1038/nrclinonc.2016.206.
66. Manic G, Obrist F, Kroemer G, Vitale I, and Galluzzi L (2014). Chloroquine and hydroxychloroquine for cancer therapy. Mol Cell Oncol 1, e29911. 10.4161/mco.29911.
67. Florian MC, Dörr K, Niebel A, Daria D, Schrezenmeier H, Rojewski M, Filippi MD, Hasenberg A, Gunzer M, Scharffetter-Kochanek K, et al. (2012). Cdc42 activity regulates hematopoietic stem cell aging and rejuvenation. Cell Stem Cell 10, 520–530. 10.1016/j.stem.2012.04.007. [PubMed: 22560076]
68. Kühn R, Schwenk F, Aguet M, and Rajewsky K (1995). Inducible gene targeting in mice. Science 269, 1427–1429. 10.1126/science.7660125. [PubMed: 7660125]
69. Fang X, Bogomolovas J, Wu T, Zhang W, Liu C, Veevers J, Stroud MJ, Zhang Z, Ma X, Mu Y, et al. (2017). Loss-of-function mutations in co-chaperone BAG3 destabilize small HSPs and cause cardiomyopathy. J Clin Invest 127, 3189–3200. 10.1172/jci94310. [PubMed: 28737513]
70. Akashi K, Traver D, Miyamoto T, and Weissman IL (2000). A clonogenic common myeloid progenitor that gives rise to all myeloid lineages. Nature 404, 193–197. 10.1038/35004599. [PubMed: 10724173]
71. Kikuchi K, Kasai H, Watanabe A, Lai AY, and Kondo M (2008). IL-7 specifies B cell fate at the common lymphoid progenitor to pre-proB transition stage by maintaining early B cell factor expression. J Immunol 181, 383–392. 10.4049/jimmunol.181.1.383. [PubMed: 18566404]
72. Kondo M, Weissman IL, and Akashi K (1997). Identification of clonogenic common lymphoid progenitors in mouse bone marrow. Cell 91, 661–672. 10.1016/s0092-8674(00)80453-5. [PubMed: 9393859]
73. Ames K, Kaur I, Shi Y, Tong M, Sinclair T, Hemmati S, Glushakow-Smith SG, Tein E, Gurska L, Dubin R, et al. (2020). Deletion of PI3-Kinase Promotes Myelodysplasia Through Dysregulation of Autophagy in Hematopoietic Stem Cells. bioRxiv, 2020.2012.2004.412593. 10.1101/2020.12.04.412593.

74. Picelli S, Faridani OR, Björklund AK, Winberg G, Sagasser S, and Sandberg R (2014). Full-length RNA-seq from single cells using Smart-seq2. Nat Protoc 9, 171–181. 10.1038/nprot.2014.006. [PubMed: 24385147]

75. Dobin A, Davis CA, Schlesinger F, Drenkow J, Zaleski C, Jha S, Batut P, Chaisson M, and Gingeras TR (2013). STAR: ultrafast universal RNA-seq aligner. Bioinformatics 29, 15–21. 10.1093/bioinformatics/bts635. [PubMed: 23104886]

76. Schmieder R., and Edwards R. (2011). Quality control and preprocessing of metagenomic datasets. Bioinformatics 27, 863–864. 10.1093/bioinformatics/btr026. [PubMed: 21278185]

77. Li H, Handsaker B, Wysoker A, Fennell T, Ruan J, Homer N, Marth G, Abecasis G, and Durbin R (2009). The Sequence Alignment/Map format and SAMtools. Bioinformatics 25, 2078–2079. 10.1093/bioinformatics/btp352. [PubMed: 19505943]

78. Liao Y, Smyth GK, and Shi W (2014). featureCounts: an efficient general purpose program for assigning sequence reads to genomic features. Bioinformatics 30, 923–930. 10.1093/bioinformatics/btt656. [PubMed: 24227677]

79. Love MI, Huber W, and Anders S (2014). Moderated estimation of fold change and dispersion for RNA-seq data with DESeq2. Genome Biol 15, 550. 10.1186/s13059-014-0550-8. [PubMed: 25516281]

Highlights

- Ex vivo cultured HSCs rapidly and massively increase protein synthesis
- Hsf1 is activated in culture to promote ex vivo HSC maintenance and proteostasis
- Small molecule activators of Hsf1 enhance HSC maintenance and fitness in culture
- Hsf1 is activated in aging HSCs in vivo to promote proteostasis and fitness

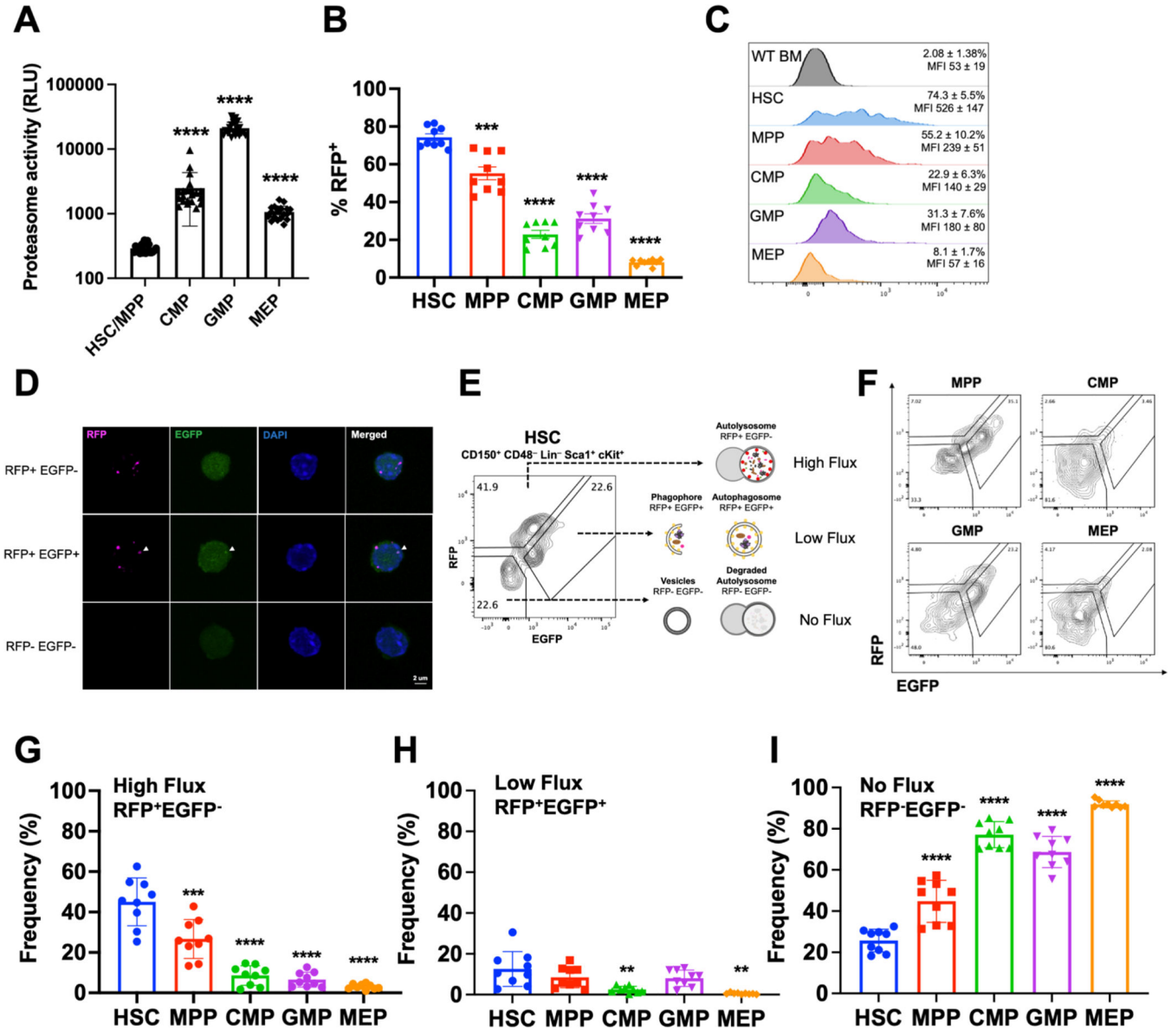

Figure 1.

HSCs exhibit high levels of autophagy in vivo.

A. Proteasome activity in HSCs/MPPs (CD48^{-}LSK), CMPs, GMPs, and MEPs measured in relative luminescence units (n=21–22 replicates in 8 experiments).

B. Autophagic activity in HSCs, MPPs, and myeloid progenitors measured by frequency of RFP^{+} cells in CAG-RFP-EGFP-LC3 mice (n=9 mice from 3 experiments).

C. Representative histograms for RFP expression in bone marrow cells from wildtype mice and HSCs, MPPs, CMPs, GMPs, and MEPs from CAG-RFP-EGFP-LC3 mice (n=9 mice from 3 experiments). Mean frequency and fluorescence intensity of individual mice are shown ± standard deviation (SD).

D. Representative confocal images of FACS isolated RFP^{+}EGFP^{-} (high flux), RFP^{+}EGFP^{+} (low flux), and RFP^{-}EGFP^{-} (undetectable flux) HSCs.

E-F Flow cytometry gating strategy for identifying high (RFP^+EGFP^-), low (RFP^+EGFP^+), and no flux (RFP^-EGFP^-) autophagy HSCs (E) or progenitors (F) in CAG-RFP-EGFP-LC3 mice.

G-I Frequency of cells undergoing high (G), low (H), and no autophagic flux (I) in CAG-RFP-EGFP-LC3 mice determined by flow cytometry (n=9 mice from 3 experiments).

Data show individual replicates and mean ± SD in A-B and G-I. Data were assessed using a student's t-test (A) or a one-way ANOVA with Dunnett's test relative to HSCs (B, G-I). **P≤ 0.01, ***P≤ 0.001, ****P≤ 0.0001.

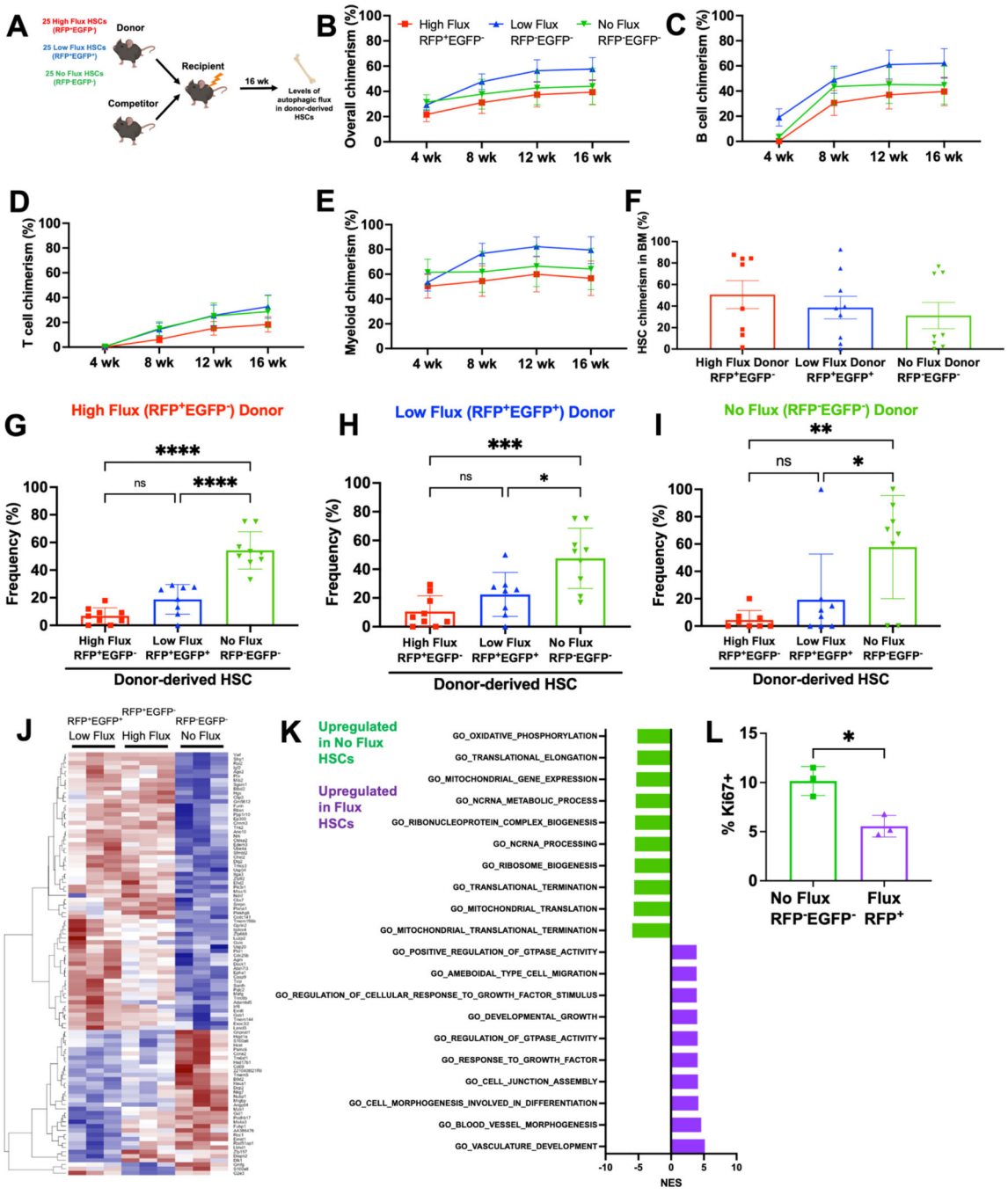

Figure 2.

HSCs dynamically transition between autophagic flux states.

A Schematic for competitive transplantation of RFP^{+}EGFP^{-} high flux, RFP^{+}EGFP^{+} low flux, and RFP^{-}EGFP^{-} no flux HSCs into irradiated recipients.

B-E Donor hematopoietic (B), B (C), T (D), and myeloid (E) cell engraftment in peripheral blood of mice receiving 25 RFP^{+}EGFP^{-} high flux, RFP^{+}EGFP^{+} low flux, or RFP^{-}EGFP^{-} no flux HSCs with 3×10^{5} bone marrow cells (n=10–13 recipients/HSC subset in 3 experiments).

F-I HSC engraftment (F) and autophagic activity (G-I) in the bone marrow of mice from transplants in B-E 16 weeks post-transplantation (n=8–9 recipients/HSC subset in 3 experiments).

J Heat map comparing differentially expressed transcripts between $RFP^{+}EGFP^{-}$, $RFP^{+}EGFP^{+}$, and $RFP^{-}EGFP^{-}$ HSCs (≥1.5-fold change, Padj<0.05, n=3).

K Normalized enrichment scores from GSEA of most upregulated and downregulated pathways in autophagic versus non-autophagic HSCs.

L Frequency of $Ki67^{+}$ $RFP^{-}EGFP^{-}$ or RFP^{+} $CD48^{-}$LSK HSC/MPPs (n=3).

Data show individual mice (F-I, L) and/or mean (B-I, L) ± SEM (B-E) or SD (F-I, L). Data were assessed by a one-way repeated measures (B-E) or ordinary (F-I) ANOVA followed by Tukey's test, or student's t-test (L). *P≤ 0.05, **P≤ 0.01, ***P≤ 0.001, ****P≤ 0.0001.

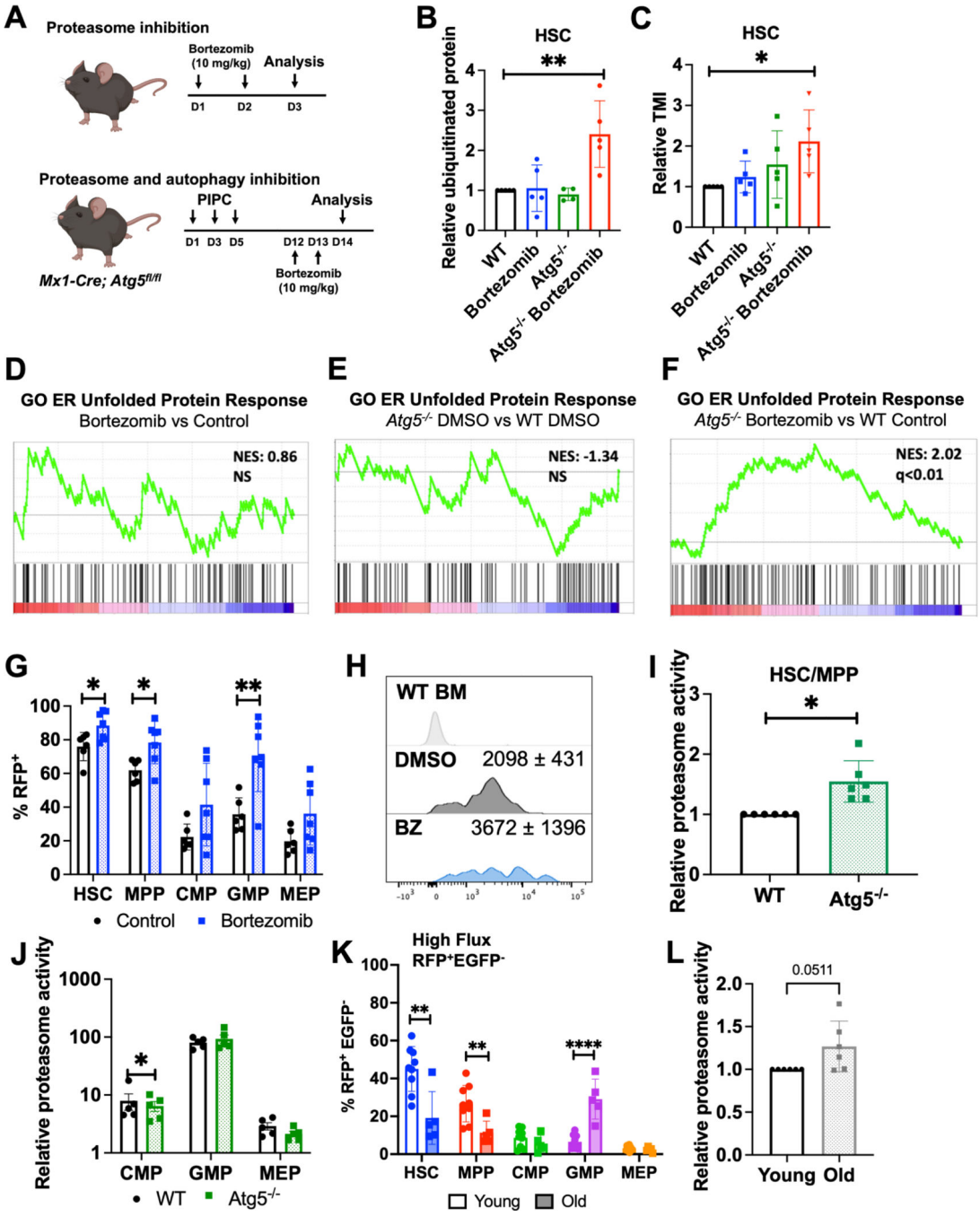

Figure 3.

Proteasome and autophagy collaborate to clear unfolded/misfolded proteins.

A Strategy for inhibition of proteasome and simultaneous inhibition of proteasome and autophagy in vivo.

B-C Relative misfolded (ubiquitinated) and unfolded (TMI) protein in HSCs from vehicle (DMSO)-treated wildtype (WT), vehicle-treated *Atg5*$^{-/-}$, WT bortezomib-treated, and *Atg5*$^{-/-}$ bortezomib-treated mice (n=5 from 5 experiments).

D-F Gene set enrichment plots showing that a UPR gene set is not increased in HSCs when proteasome (D) or autophagy (E) alone are inhibited but significantly upregulated when both pathways are inhibited (F) in vivo (n=3).

G Frequency of RFP^+ autophagic cells after bortezomib treatment in CAG-RFP-EGFP-LC3 mice (n=6 from 3 experiments).

H Representative histograms and mean fluorescence intensity ± SD of RFP in WT bone marrow cells and bortezomib-treated or control CAG-RFP-EGFP-LC3 HSCs.

I-J Relative proteasome activity in WT or *Atg5*$^{-/-}$ $CD48^-$LSK HSC/MPPs (I) and restricted progenitors (J) (n=6 from 6 experiments).

K Frequency of cells with high autophagic flux (RFP^+EGFP^-) in young (3 month) and old (22–24 month) CAG-RFP-EGFP-LC3 mice (n=5–9).

L Relative proteasome activity in young (3 month) and old (22–24 month) $CD48^-$LSK HSC/MPPs (n=6 from 6 experiments).

Data show individual mice and means ± SD (B-C, G, I-L). Data were assessed by ordinary one-way ANOVA with Dunnett's test relative to WT (B-C) or student's t-test (G, I-L). *P≤ 0.05, **P≤ 0.01, ***P≤ 0.001, ****P≤ 0.0001.

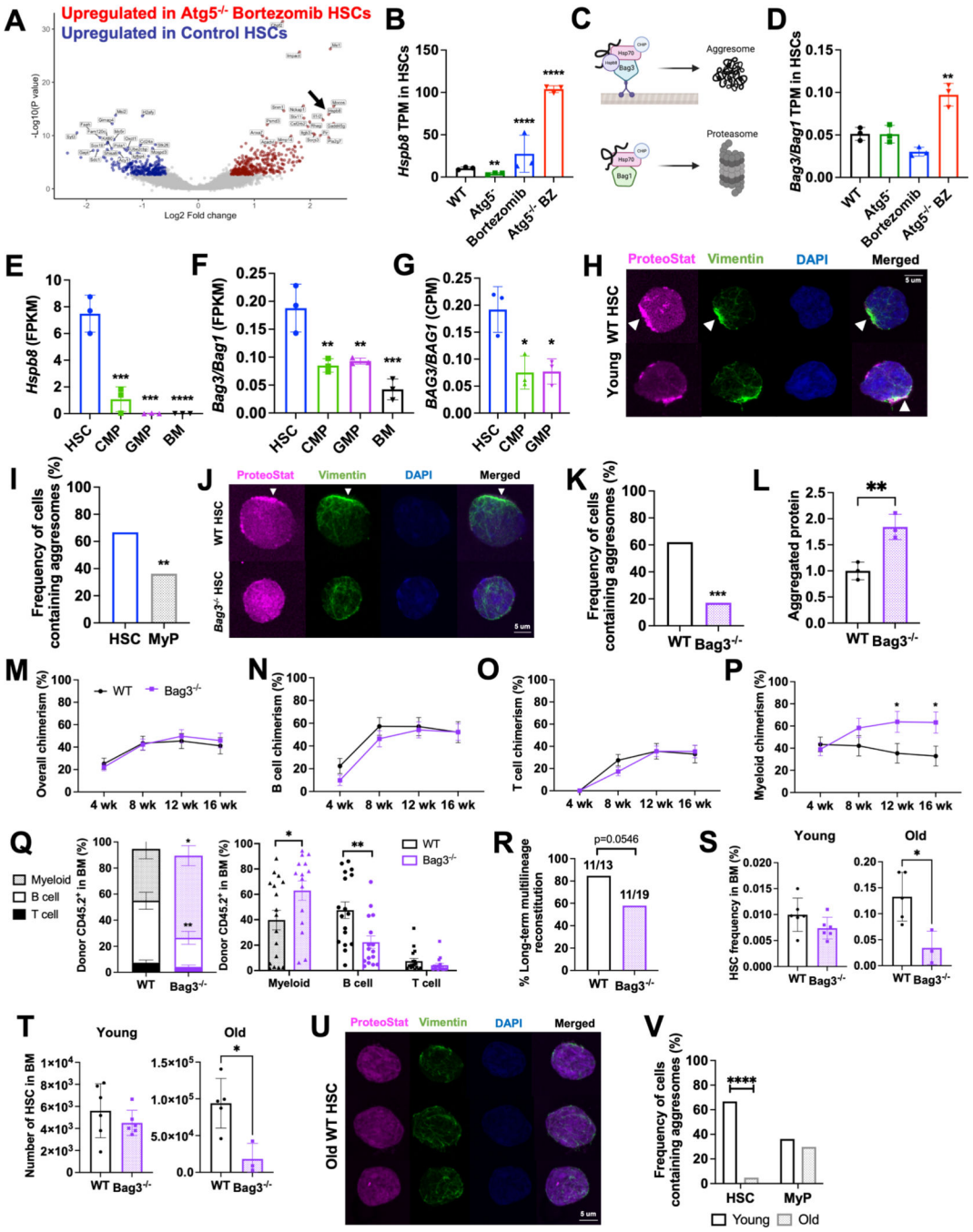

Figure 4.

HSCs preferentially traffic misfolded proteins to aggresomes for removal by aggrephagy.

A Volcano plot highlighting 20 most upregulated (red) and downregulated (blue) genes in HSCs from bortezomib-treated *Atg5*$^{-/-}$ mice relative to vehicle (DMSO)-treated wildtype (WT) HSCs.

B,D *Hspb8* (B) and ratio of *Bag3*/*Bag1* (D) expression in vehicle-treated WT, vehicle-treated *Atg5*$^{-/-}$, bortezomib-treated WT, and bortezomib-treated *Atg5*$^{-/-}$ HSCs (n=3). Data show mean transcripts per million (TPM).

C The Bag3 complex delivers protein substrates to aggresomes by microtubule-dependent retrograde transport while the Bag1 complex shuttles unfolded/misfolded proteins to the proteasome.

D Ratio of *Bag3*/*Bag1* expression in vehicle-treated WT, vehicle-treated *Atg5*$^{-/-}$, bortezomib-treated WT, and bortezomib-treated *Atg5*$^{-/-}$ HSCs (n=3).

E-F *Hspb8* (E) and ratio of *Bag3/Bag1* (F) expression in HSCs, progenitors, and unfractionated bone marrow (BM) at steady state in vivo (n=3).

G Ratio of *BAG3/BAG1* expression in human cord blood-derived HSCs, CMPs and GMPs[26,46] (n=3). Data show mean counts per million.

H Representative images of young adult HSCs containing aggresomes (polarized, perinuclear co-localization of ProteoStat with vimentin).

I Frequency of young adult HSCs and myeloid progenitors (MyP; CD127^{-}Lineage^{-}Sca-1c-kit^{+}) containing aggresomes (n=36–47 cells/population).

J Representative images of aggresome staining in WT and *Bag3*$^{-/-}$ HSCs.

K Frequency of WT and *Bag3*$^{-/-}$ HSCs containing aggresomes (n=17–62 HSCs).

L Aggregated proteins (relative ProteoStat MFI) in WT and *Bag3*$^{-/-}$ HSCs (n=3).

M-P Frequency of donor-derived hematopoietic (M), B (N), T (O), and myeloid (P) cell chimerism when 25 WT or *Bag3*$^{-/-}$ HSCs were transplanted with 3×10^5 bone marrow cells into irradiated mice (n=16 recipients/genotype from 4 experiments).

Q Lineage distribution of donor-derived cells from transplants in (M-P). Breakdown by individual recipient is shown in the right panel.

R Frequency of secondary recipients of WT and *Bag3*$^{-/-}$ HSCs that exhibit long-term multilineage reconstitution (n=13–19 recipients/genotype from 3 experiments).

S-T Frequency (S) and number (T) of HSCs in the bone marrow (1 femur + 1 tibia) of young (2–3 month) and old (22–25 month) WT and *Bag3*$^{-/-}$ mice (n=3–6).

U Representative images of aggresome staining in old (22–24 month) WT HSCs.

V Frequency of HSCs and myeloid progenitors containing aggresomes in young (3 month) and old (22–24 month) mice (n= 21–84).

Data show individual replicates/mice and/or means ± SD (B,D–G, L, Q, S–T) or SEM (M–P). Data were assessed by ordinary one-way ANOVA with Dunnett's test relative to WT (D–G), chisquared test (I, K, R, V) or student's t-test (L–Q, S–T). *P≤ 0.05, **P≤ 0.01, ***P≤ 0.001, ****P≤ 0.0001.

KEY RESOURCES TABLE

REAGENT or RESOURCE	SOURCE	IDENTIFIER
Antibodies		
APC Anti-mouse CD3ε (17A2)	BioLegend	Cat #100236; RRID:AB_2561456
FITC Anti-mouse CD3ε (17A2)	BioLegend	Cat #100204; RRID:AB_312661
PE Anti-mouse CD3ε (17A2)	BioLegend	Cat #100206; RRID:AB_312663
Brilliant Violet 650 Anti-mouse CD3ε (17A2)	BioLegend	Cat #100229 RRID: AB_11204249
APC Anti-mouse CD4 (GK1.5)	BioLegend	Cat #100412; RRID:AB_312697
FITC Anti-mouse CD4 (GK1.5)	BioLegend	Cat #100406; RRID:AB_312691
PE Anti-mouse CD4 (GK1.5)	BioLegend	Cat #100408; RRID:AB_312693
APC Anti-mouse CD5 (53–7.3)	BioLegend	Cat #100626; RRID:AB_2563929
FITC Anti-mouse CD5 (53–7.3)	BioLegend	Cat #100606; RRID:AB_312735
PE Anti-mouse CD5 (53–7.3)	BioLegend	Cat #100608; RRID:AB_312737
APC Anti-mouse CD8α (53–6.7)	eBioscience	Cat #17–0081-82; RRID:AB_469335
FITC Anti-mouse CD8α (53–6.7)	eBioscience	Cat #11–0081-85; RRID:AB_464916
PE Anti-mouse CD8α (53–6.7)	eBioscience	Cat #12–0081-83; RRID:AB_465531
APC Anti-mouse CD11b (M1/70)	eBioscience	Cat #17–0112-82; RRID:AB_469343
APC efluor780 Anti-mouse CD11b (M1/70)	eBioscience	Cat #47–0112-82; RRID:AB_1603093
FITC Anti-mouse CD11b (M1/70)	eBioscience	Cat #12–0112-83; RRID:AB_2734870
PE Anti-mouse CD11b (M1/70)	eBioscience	Cat #11–0112-85; RRID:AB_464936
PE/Cy7 Anti-mouse CD16/32 (FcγRII/III; 93)	BioLegend	Cat #101318; RRID:AB_2104156
PerCP/Cy5.5 Anti-mouse CD16/32 (FcγRII/III; 93)	BioLegend	Cat #101324; RRID:AB_1877267
Biotin Anti-mouse CD34 (RAM34)	eBioscience	Cat #13–0341-85; RRID:AB_466426
Alexa Fluor 700 Anti-mouse CD34 (RAM34)	eBioscience	Cat #56–0341-82; RRID:AB_493998
FITC Anti-mouse CD34 (RAM34)	eBioscience	Cat #11–0341-85; RRID:AB_465022
APC Anti-mouse CD41 (MWReg30)	Biolegend	Cat #133913; RRID:AB_1112675 1
FITC Anti-mouse CD43 (R2/60)	eBioscience	Cat #11–0431-85; RRID:AB_465041
PE Anti-mouse CD43 (R2/60)	eBioscience	Cat #12–0431-83; RRID:AB_465660
APC eFluor 780 Anti-mouse CD45.1 (A20)	eBioscience	Cat #47–0453-82; RRID:AB_1582228
Alexa Fluor 700 Anti-mouse CD45.2 (104)	BioLegend	Cat #109822; RRID:AB_493731
FITC Anti-mouse CD45.2 (104)	BioLegend	Cat #109806; RRID:AB_313443

REAGENT or RESOURCE	SOURCE	IDENTIFIER
APC Anti-mouse CD45R (B220) (RA3–6B2)	eBioscience	Cat #17–0452-83; RRID:AB_469396
FITC Anti-mouse CD45R (B220) (RA3–6B2)	eBioscience	Cat #11–0452-85; RRID:AB_465055
PE Anti-mouse CD45R (B220) (RA3–6B2)	eBioscience	Cat #12–0452-85; RRID:AB_465673
PerCP-Cyanine5 Anti-mouse CD45R (B220) (RA3–6B2)	eBioscience	Cat #45–0452-82; RRID:AB_1107006
APC Anti-mouse CD48 (HM48–1)	BioLegend	Cat #103412; RRID:AB_571997
FITC Anti-mouse CD48 (HM48–1)	BioLegend	Cat #103404; RRID:AB_313019
PE Anti-mouse CD48 (HM48–1)	BioLegend	Cat #103406; RRID:AB_313021
PE/Cy7 Anti-mouse CD48 (HM48	BioLegend	Cat #103424; RRID:AB_2075049
FITC Anti-mouse CD71 (R17217)	eBioscience	Cat #11–0711-85; RRID:AB_465125
APC Anti-mouse CD117 (cKit) (2B8)	eBioscience	Cat #17–1171-83; RRID:AB_469431
APC eFluor 780 Anti-mouse CD117 (cKit) (2B8)	eBioscience	Cat #47–1171-82; RRID:AB_1272177
PE-Cyanine7 Anti-mouse CD117 (cKit) (2B8)	eBioscience	Cat #25–1171-82; RRID:AB_469644
PE Anti-mouse CD127 (IL7Rα; A7R34)	BioLegend	Cat #135010; RRID:AB_1937251
APC Anti-mouse CD150 (TC15–12F12.2)	BioLegend	Cat #115910; RRID:AB_493460
PE Anti-mouse CD150 (TC15–12F12.2)	BioLegend	Cat #115904; RRID:AB_313683
PE-Cyanine7 Anti-mouse CD150 (TC15–12F12.2)	BioLegend	Cat #115914; RRID:AB_439797
Brilliant Violet 650 Anti-mouse CD150 (TC15–12F12.2)	BioLegend	Cat #115931 RRID: AB_2562402
APC Anti-mouse Ter119 (TER-119)	Biolegend	Cat #116212; RRID:AB_313713
FITC Anti-mouse Ter119 (TER-119)	Biolegend	Cat #116206; RRID:AB_313709
PE Ter119 (TER-119)	Biolegend	Cat #116208; RRID:AB_313709
APC Anti-mouse Sca-1 (D7, E13–161.7)\	eBioscience	Cat #17–5981-82; RRID:AB_469487
Alexa Fluor 700 Anti-mouse Sca-1 (D7, E13–161.7)	eBioscience	Cat #56–5981-82; RRID:AB_657836
FITC Anti-mouse Sca-1 (D7, E13–161.7)	eBioscience	Cat #11–5981-85; RRID:AB_465334
PerCp-Cyanine5.5 Anti-mouse Sca-1 (D7, E13–161.7)	eBioscience	Cat #45–5981-82; RRID:AB_914372
APC Anti-mouse Gr-1 (RB6–8C5)	BioLegend	Cat #108412; RRID:AB_313377
FITC Anti-mouse Gr-1 (RB6–8C5)	BioLegend	Cat #108406; RRID:AB_313371
PE Anti-mouse Gr-1 (RB6–8C5)	BioLegend	Cat #108408; RRID:AB_313373
PE/Cy7 Anti-mouse Gr-1 (RB6–8C5)	BioLegend	Cat #108416; RRID:AB_312663
APC Anti-mouse IgM (II/41)	eBioscience	Cat #17–5790-82; RRID:AB_469458
PE Anti-mouse IgM (II/41)	eBioscience	Cat #12–5790-83; RRID:AB_465941

REAGENT or RESOURCE	SOURCE	IDENTIFIER
Recombinant Alexa Fluor 647 Anti-SQSTM1/p62 antibody (EPR4844)	Abcam	Cat # ab194721
Anti-vimentin antibody	Millipore Sigma	Cat #AB5733
Goat anti-chicken IgY (H&L) Alexa Fluor 488	Invitrogen	Cat #A-11039
Chemicals, Peptides, and Recombinant Proteins		
PIPC	GE Healthcare Biosciences Corp	Cat #27473201
Anti-mouse CD117 microbeads	Miltenyi	Cat #130–091-224
2-mercaptoethanol	Sigma	Cat #M3148
Heat-inactivated bovine serum	Gibco	Cat #26170043
DMSO	Sigma	Cat #D2650
Baytril	Covetrus	Cat #37713
Ammonium chloride potassium buffer	Covetrus	Cat #37713
Paraformaldehyde	Affymetrix	Cat #19943
4% paraformaldehyde aqueous solution	Electron Microscopy Sciences	Cat #157–4
PBS	Corning	Cat #MT21040CV
Tween 20	Sigma	Cat #P9416
4’,6-diamidino-2-phenylindole (DAPI)	Life Technologies	Cat #62247
Saponin	Sigma	Cat #47036
Fetal Bovine Serum	Life Technologies	Cat #16000044
Bortezomib	Cell Signaling	Cat #2204S
Critical Commercial Assays		
Proteasome-Glo chymotrypsin-like cell based assay	Promega	Cat #G8660
RNeasy Plus Micro Kit	Qiagen	Cat #74034
PROTEOSTAT Aggresome detection kit	Enzo	Cat #ENZ-51035-K100
ProLong Diamond Antifade Mountant	Thermo	Cat #P36965
Deposited Data		
RNA-sequencing data	This manuscript	GEO GSE179415
RNA-sequencing data for human HSCs and progenitors	Xie et al, 2019	GEO: GSE125345
RNA-sequencing data for human HSCs and progenitors	Laurenti et al, 2013	GEO: GSE42414
RNA-sequencing data for mouse HSCs and progenitors	Signer et al, 2016	N/A
Experimental Models: Organisms/Strains		
Mouse: B6: C57BL/6J	The Jackson Laboratory	Cat #000664; RRID:IMSR_JAX:0 00664
Mouse: B6SJL: B6.SJL	The Jackson Laboratory	Cat #002014; RRID:IMSR_JAX:0 02014
Mouse: C57BL/6-Tg(CAG-RFP/EGFP/Map1lc3b)1Hill/J	The Jackson Laboratory	Cat #027139; RRID:IMSR_JAX:0 27139
Mouse: *Bag3*$^{fl/fl}$	Fang et al, 2017	N/A
Mouse: *Atg5*$^{fl/fl}$	Hara et al, 2006	N/A

REAGENT or RESOURCE	SOURCE	IDENTIFIER
Mouse: *Mx1-Cre*: B6.Cg-Tg(Mx1-cre)1Cgn/J	The Jackson Laboratory	Cat #003556 RRID:IMSR_JAX:003556
Software and Algorithms		
FlowJo	FlowJo, LLC	https://www.flowjo.com/solutions/flowjo/downloads
FACSDiva	BD Bioscience	https://www.bdbiosciences.com/enus/products/software/instrumentsoftware/bdfacsdiva-software
Prism 8	GraphPad	https://www.graphpad.com/scientific-software/prism/
ImageJ	NIH	https://imagej.nih.gov/ij/
Image Lab 6.0.1	Bio-Rad	https://www.biorad.com/enus/product/image-lab-software?ID=KRE6P5E8Z
TopHat 1.4.1	JHU CCB	https://ccb.jhu.edu/software/tophat/downloads/
STAR 2.6.1	N/A	https://github.com/alexdobin/STAR
PRINSEQ Lite 0.20.3	N/A	https://sourceforge.net/projects/prinseq/files/standalone/
Htseq-count 0.7.1	N/A	https://htseq.readthedocs.io/en/master/install.html
featureCounts 1.6.5	N/A	https://sourceforge.net/projects/subre ad/files/subread1.6.5/
Bioconductor package DESeq2 1.24.0	Bioconductor	https://git.bioconductor.org/packages/DESeq2
Matplotlib	J.D Hunter, 2007	https://matplotlib.org/stable/index.html
ELDASoftware	Hu and Smyth, 2009	https://bioinf.wehi.edu.au/software/elda/
ZEN (black edition)	Zeiss	https://www.zeiss.com/microscopy/en/products/software/zeiss-zen.html
ZEN (blue edition)	Zeiss	https://www.zeiss.com/microscopy/en/products/software/zeiss-zen.html